UNIVERSITY OF OKLAHOMA

GRADUATE COLLEGE

ADDITIVE MANUFACTURING OF TI-64 USING SELECTIVE LASER MELTING

A THESIS

SUBMITTED TO THE GRADUATE FACULTY

in partial fulfillment of the requirements for the

Degree of

MASTER OF SCIENCE

By

CAYLIN NIMMO

Norman, Oklahoma

2024

ADDITIVE MANUFACTURING OF TI-64 USING SELECTIVE LASER MELTING

A THESIS APPROVED FOR THE

SCHOOL OF AEROSPACE AND MECHANICAL ENGINEERING

BY THE COMMITTEE CONSISTING OF

Dr. Christopher Billings, Chair

Dr. Yingtao Liu

Dr. Zahed Siddique

© Copyright by CAYLIN NIMMO 2024
All Rights Reserved.

Acknowledgements

First, I want to offer my gratitude to the Sooner Advanced Manufacturing Laboratory (SAML) team and the Oklahoma Aerospace and Defense Innovation Institute. Specifically, I want to thank Dr. Yingtao Liu for supporting me through the accelerated master's degree. He provided me guidance when I faced challenging problems and removed barriers when road-blocks appeared. Your adaptability, responsiveness and work ethic are the reasons I can proudly submit this work. Additionally, I would like to thank Dr. Christopher Billings for being a member of my thesis committee and for all his expertise over the last year. There have been many ups, downs, delays, and hurdles, but you have been a kind and patient mentor at every step of the journey. I aspire to be an engineer of your caliber eventually. Similarly, John Auld has worked tirelessly to keep the SAML moving forward and on a positive trajectory. Without your work behind the scenes, I would have had far fewer opportunities to try new hard things and contribute meaningfully to the team. Additionally, I would like to thank Dr. Zahed Siddique for offering his time to be a member of my thesis committee and for creating opportunities for students like me to engage with cutting edge research at the University of Oklahoma.

I would also like to thank my lab mates, James Totah, Joshua Hall, Ben Sherwood, Elijah Personette, Peter Vu, Conner Lawrence, and Kyle Brownlee. Without your encouragement, brainstorming capabilities, and guidance I would have struggled through the graduate program. Thank you also to my friends who supported me outside of the classroom; Adam Bicak, Sohil Desai, Wink Winkle, Wesley May, Devyn Lutz, Hannah Lang, Rae Lane, Kira Riggs, Anthony Barcio, Braden White, Blake Adkins, and the E-Club team. You helped keep me focused and excited about being here each day.

Additionally, I need to offer my gratitude to the professors and teachers who gave me the tools I needed to face any problem. Dr. Ramkumar Parthasarathy, you taught me just as much about professionalism and diligence as you did about propulsion systems and wind tunnels. I will forever respond to your emails within 24 hours. Dr. Diogo Sanchez, your excitement for astrodynamics and perspective brought life back into my academic career when I needed it most. Dr. Kim Wolfenbarger, Dr. Christopher Childers, General Donald Wetekam, General Jerry Holmes, Kirby Wilkerson, and David Snell, you have been exceptional mentors that put me in the right place at the right time. Your guidance and wisdom have forever altered my life for the better.

Finally, my attendance in higher education would have been impossible without the support of my family, sponsors, and donors to the Gallogly College of Engineering. I can only hope to pay my debt forward and do for others what you have done for me.

Table of Contents

Table of Figures

Table of Tables

Abstract

Selective Laser Melting (SLM) is an Additive Manufacturing (AM) process that is seeing adoption in many engineering industries, namely in biomedical, automotive, and aerospace applications. In this work, the capabilities of the General Electric (GE) Additive Concept M2 Series 5 Titanium Ti-64 Grade 23 SLM printer are characterized in a preliminary study to guide future research and processes at the Sooner Additive Manufacturing Laboratory (SAML). Ti-64 (90% titanium, 6% aluminum, 4% vanadium by weight) AM has become more accessible in the last decade and is of particular interest to the United States Air Force for fabricating replacement parts for aging aircraft. This work focuses on reviewing the Powder Bed Fusion (PBF) process and determining the bulk tensile properties of horizontally printed specimens using GE's provided parameters while expanding the capabilities of the SAML to prepare it for additional testing. As printed samples were compared to all 3 of the Stress Relief (SR) options provided by GE alongside a study to evaluate the potential for shot peening using resources readily available in the laboratory. Samples were evaluated using Digital Image Correlation (DIC) during the loading processes and a universal testing system. Samples were shown to present properties similar to that of the provided GE specifications, but fell short of the published values for as printed and SR3 samples for the Balanced Parameter 114. In-house polishing processes were expanded to successfully present Ti-64 grain structures under optical microscopy and Scanning Electron Microscopy (SEM) by decreasing the final polishing particle size to 0.02 μm and including additional particle sizes during preparation (9 μm, 6 μm, 3 μm, 1 μm, 0.05 μm, 0.02 μm). Future work should and will include a larger sample size for each specimen type and utilize ASTM E8M specimens.

CUI

Chapter 1: Introduction

1.1 Review of Additive Manufacturing

Additive Manufacturing (AM) or 3D printing has seen increasing commercialization across many industries. Affordable Fused Deposition Modeling (FDM) have become a staple for crafty hobbyists and more advanced printing processes have seen increasing adoption in manufacturing industries. Chiefly, AM is becoming much more prevalent in Aerospace, Automotive, and Biomedical applications [1]. AM can be utilized in many different way, but is primarily leveraged for rapid prototyping, creating low production- highly specialized parts, or to create complex geometries that cannot be made through traditional manufacturing [1], [2], [3].

While there is a broad range of AM processes, they are normally described by the method of material deposition. FDM printing normally pressed some type of thermoplastic, be it pellets or a spool of filament, into a heating element and subsequently extruded through a nozzle. FDM printing is relatively cheap when compared to other AM processes such as Powder Bed Fusion (PBF), where these machines are more limited to commercial or research applications because of restrictive costs. In 2015, the American Society for Testing and Materials (ASTM) categorized AM into 7 process methodologies: Binder jetting, directed energy deposition, material extrusion, material jetting, powder bed fusion, sheet lamination, and vat photopolymerization. Each of the methodologies tends to specialize in producing parts out of a subset of materials. For example, in the case of material extrusion, it has limited access to forming components out of metals, while PBF has access to an entire range of materials.

Regardless of the selected manufacturing method, all AM techniques abide by the same generalized process. 1: Computer Aided Design (CAD) tools are used to create a desired part geometry. This can be done with professional or amateur software, but the model must have 3-dimensional geometry or a surface. 2: The body or surface is converted into a STL file, which describes the geometry, enclosed surfaces, and center of the CAD. 3: The STL is processed by a slicing software or the 3D printer in preparation for printing. The part geometry is normally partitioned into a series of layers and a printer "path" is determined based on each layer. This is also where additional components such as supports or infill may be added to ensure the part is compatible with the printing methodology and may be successfully printed. 4: The printing machine is prepared for the building process by providing it with the necessary materials, consumables, or maintenance to begin the printing process. 5: The printer is left to print the desired part, normally unattended or under limited monitoring. Normally, the printing process creates a series of thin material layers that are stacked on each other to create a 3-dimensional object. 6: The printed component is removed from the machine and build area. This can be relatively simple for some machines or require the use of protective equipment and tooling for others. 7: The part is processed after its removal from the machine. In some cases this involves cleaning, a type of surface or heat treatment, or the removal of additional components such as supports. 8: Finally, the part is ready for use, unless it requires additional processing such as machining operations, the insertion of threaded inserts or threads, and paints.

The AM process originally appears to be completely hands free, but it is often more engaging than meets the eye for more complex manufacturing methods. Printers, especially high-end machines, require maintenance, specialized operating conditions, and periodic recalibration. AM sits at the intersection of manufacturing and material science. Since these processes do not

adhere to traditional manufacturing standards and the machines may present deviations from device to device, there is still hesitancy to adopt AM for some critical applications. Technical societies, companies, and governing bodies have opted to pursue engineering company's age-old practice of repeated and rigorous testing of components parts with these new technologies. To add increasing complexity, 3D printing materials often require specialized processing or handling before they can be used in the printing process. These may require environments that provide unique care, be caustic, or have expiration dates that must be accounted for [1].

1.1.1 Powder Bed fusion

While these generalizations are true for all printing methods, the most relevant printing process to this work is powder bed fusion, which has seen increased application across the aerospace, automotive, and biomedical industries [2]. One of the earliest AM processes, PBF was first developed alongside Selective Laser Sintering (SLS) in the late 1980's at the University of Texas – Austin by Dr. Carl Deckard [4]. Deckard's original design serves as a baseline for all PBF, which all have some energy source used to fuse powder particles together, the ability to control the location and intensity of the power source along each layer, and some method for laying powder down into smooth powder layers. *Figure 1* presents a diagram that illustrates an example of the PBF process.

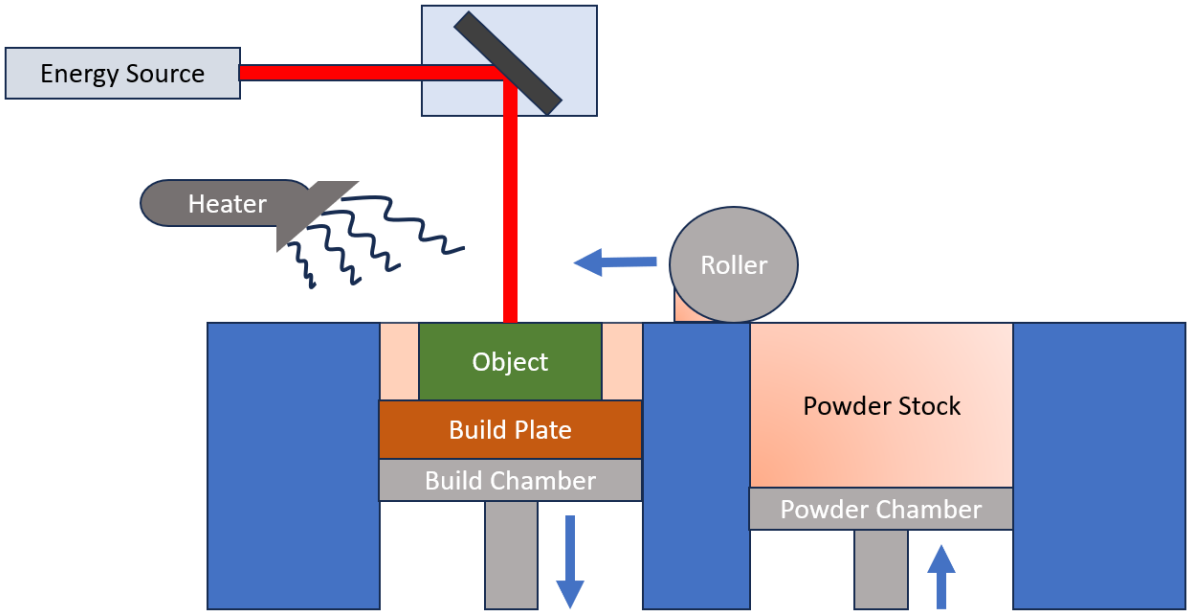

Figure 1: Generalized Powder Bed Fusion Schematic

Not all PBF methods use the same energy source, but the general characteristics are the same. Since the laser is scanned along the surface of the powder bed, the approach can be used with a variety of materials including polymers, metals, and ceramics. The energy source is used to fuse layers of powdered material together by scanning a pattern onto the surface. In many cases, the build chamber is enclosed and brought to vacuum conditions or is filled with an inert gas to minimize oxidation during the printing process. Additionally, the build chamber may operate at an increased temperature to reduce the energy required at the powder surface for melting or sintering. A roller travels from a powder source to the printing area to deposit a thin layer of powder over the printed object in an even layer. With the flat surface thermally primed, the energy source scans a pattern generated by the sliced data into the fresh powder bed. This is done with the correct power and positioning to bind together all of the power particles necessary to achieve the desired part. With the completion of a layer, the build chamber is lowered down the same thickness as a layer into the machine, while the powder chamber is elevated by the

same distance. The roller returns to the starting position and moves powder stock over the top of the build chamber to begin the process again. While not an all-encompassing list, the three most prevalent PBF processes are Selective Laser Sintering (SLS), Selective Laser Melting (SLM), and Electron Beam Melting (EBM). Three-Dimensional Printing (3DP) is another PBF method, but will not be discussed as it more closely aligns with the ASTM definition of binder jetting [1],[5].

PBF has access to almost any material that can melt and be reconstituted again, making it extremely versatile. *Table 1* serves to illustrate its diverse capabilities, outlining several of the notable materials being processed and the specific type of PBF used to do so.

Table 1: PBF Processes and Compliant Materials [5]

Process	Material Type	Materials
SLS	Polymers	Polyamide 12, GF polyamide, polystyrene
	Ceramics	Alumina, silica, zirconia, ZrB_2, bioceramic, graphite, bioglass, various sands
	Composites	Metal-metal, metal-ceramic, ceramic-ceramic, polymer-matrix, short fiber-reinforced composites
SLM	Metals	Stainless steel GP1, PH1 and 17-4, cobalt chrome MP1, Ti6Al4V, Ti6Al4V ELI and TiCP, IN718, marging steel MS1, AlSi20Mg
	Composites	Metal-metal, metal-ceramic, ceramic-ceramic, polymer-matrix, short fiber-reinforced composites
EBM	Metals	Cobalt chrome, Ti6Al4V, Ti6Al4V

Like other printing methods, polymers and composites are relatively compatible with PBF. This is especially true for thermoplastics as their insulative properties, melting point, and light-weight performance make them pragmatic to form functional printed parts from. Inversely, there is very

little use of thermosets with PBF as thermosets do not reform after melting. The thermoplastic of choice for PBF tends to be polyamide (nylon) with new materials such as PolyEtherEtherketone (PEEK) and PolyPolyArylEtherKetone (PAEK) increasing in popularity over time [6]. These thermoplastics can also be modified by incorporating fillers such as glass bead, carbon fiber, or ceramic particles in the powder [5],[7].

Metals have some of the most extensive use with PBF as metal parts can be directly manufactured using EBM and SLM or indirectly manufactured with SLS using a combination of binders, sintering, and post processing with Hot Isostatic Pressing (HIP) [5]. Utilizing sintered metals together and infiltrating them with other materials, as is the case with products such as LaserForm ST-100, offered the ability to create fully dense parts until SLM effectively rendered the technology irrelevant [8]. The direct methods fully melt down metal powder and move around the melt pool, binding material together. Fully dense AM metal parts can often have mechanical properties that exceed the capabilities of the wrought materials, making them highly desirable for certain materials. *Table 2* is an excerpt from Guo and Leu 2013 that illustrates the improved performance of Ti-64 when manufactured using AM techniques [5]. While any metal that can be welded presents a viable candidate for PBF, those that crack upon rapid cooling tend to produce subpar results [1],[9],[10].

Table 2: Material Properties of Ti64 [5]

Process	Ultimate Tensile Strength (MPa)	Yield Tensile Strength (MPa)	Elongation (%)	Elastic Modulus (GPa)
Wrought*[11]	950	880	14	113.8
EBM	1020	950	14	120
LENS	1077	973	11	-
LMD	1160	1060	6	115
SLM	~1100	~1000	~8	~120
SLS + HIP	1116.9	-	5	-
SLM† [12]	1250	1125	6	-

* Modified to specifically address purchasable ASTM Grade 5 Ti-64 per MatWeb. LLC

† Added to specifically address high density (99.98%) Ti-64

Ceramic materials are traditionally challenging to manufacture because of their hardness and thermal properties, but there has been success in PBF. Ceramics generally have more challenges than that of metals due to the reduced flowability of raw ceramic powders and their tendency to crack when exposed to high thermal stresses [13]. Successfully manufacturing ceramic parts with PBF normally involves the creation of a sintered body that is subsequently infiltrated with a filler or by incorporating ceramic particles in the printing powder as a composite. Fully dense parts have been produced exclusively through SLM, however the operating conditions for such an operation required that the ceramic be preheated to at least 1600 ℃ to stop crack formation [14].

1.1.1.1 Selective Laser Sintering and Melting

The powder material properties and their compatibility with the PBF process is essential to the success of a print, but so are the parameters and inputs of the printing operation. Laser parameters, scanning strategies, powder spreading methods, and support design are the parameters that most strongly impact SLS/SLM. A parametric study completed by Yadroitsev et

al. prioritized 3 areas of interest. Metal powder characteristics: composition, size distribution, shape, energy transfer properties, layer thickness. Laser parameters: power, spot size, beam spatial distribution, scanning velocity, and presence of inert gas. The strategy for manufacturing: scanning strategies, orientation of laser vectors, hatch spacing, and relative position between elements between planes. Recently, the interpretation for analyzing these parameters focuses on more developed characteristics. For laser parameters these would be laser spot size, melt pool dimensions, and energy density or for scanning strategies these would involve hatch spacing, adaptive vector placement, and cooling strategies within each layer [15] [16]. These parameters not only have an impact on the speed at which the part can be manufactured, but also the quality of the completed components as well [17],[18]. In addition to the laser, scanning, and powder parameters, powder bed- and chamber- temperatures must also be considered. Almost all parameters in SLM are related to, and affect one another. By increasing the bed temperature, the amount of laser power required may be decreased or vice versa. Both of these set parameters could be driven by the characteristics of the powder being processed which is impacted by the size and absorptivity of the powder.

As the core energy deposition medium, the laser device is the most critical component of SLM. While there exist a variety of lasers; gas lasers, solid-state lasers, fiber lasers, liquid lasers, and semiconductor lasers, the fiber laser is the most commonly used as it has high intensity and focus to facilitate the complete melting of the metal particles [19]. These are primarily ytterbium fiber lasers, but the specific material composition may vary [20]. Modifying laser parameters is particularly key when seeking characteristics such as high density parts (density of 99.5% or greater) [21]. While there exist extensively thorough modeling methods to describe the heat flux and deposition into the powder bed, these are often highly interrelated with the material,

scanning strategy, powder characteristics, etc. In their stead, generalized and simplified models are presented.

$$E_\rho = \frac{P}{h \times v \times t} \quad (1)$$

Where E_ρ is energy density in $\frac{J}{mm^3}$, P is laser power in W, h is hatch spacing in mm, v is the scanning velocity in $\frac{mm}{s}$, and t is the layer thickness in mm [22],[23]. Expanding the energy density equation to describe volumetric energy within a single track per Chalancon and Bourell the energy volume can be described as [24]:

$$E_V \approx \frac{P}{D \times v \times t} \quad (2)$$

Where D is the distance in mm. With (1) and (2), energy can be described in both entire areas using (1) and in single scanning vectors using (2). With the above equations, energy density is directly proportional to laser power, and inversely proportional to hatch spacing, velocity, and thickness. Energy density is the primary driver of melt pool characteristics, however, these parameters are directly impacted by both the scanning strategy and absorptivity of the powder. *Figure 2* provides a visual representation of several key characteristics of the scanning process and melt pool [1],[13],[25].

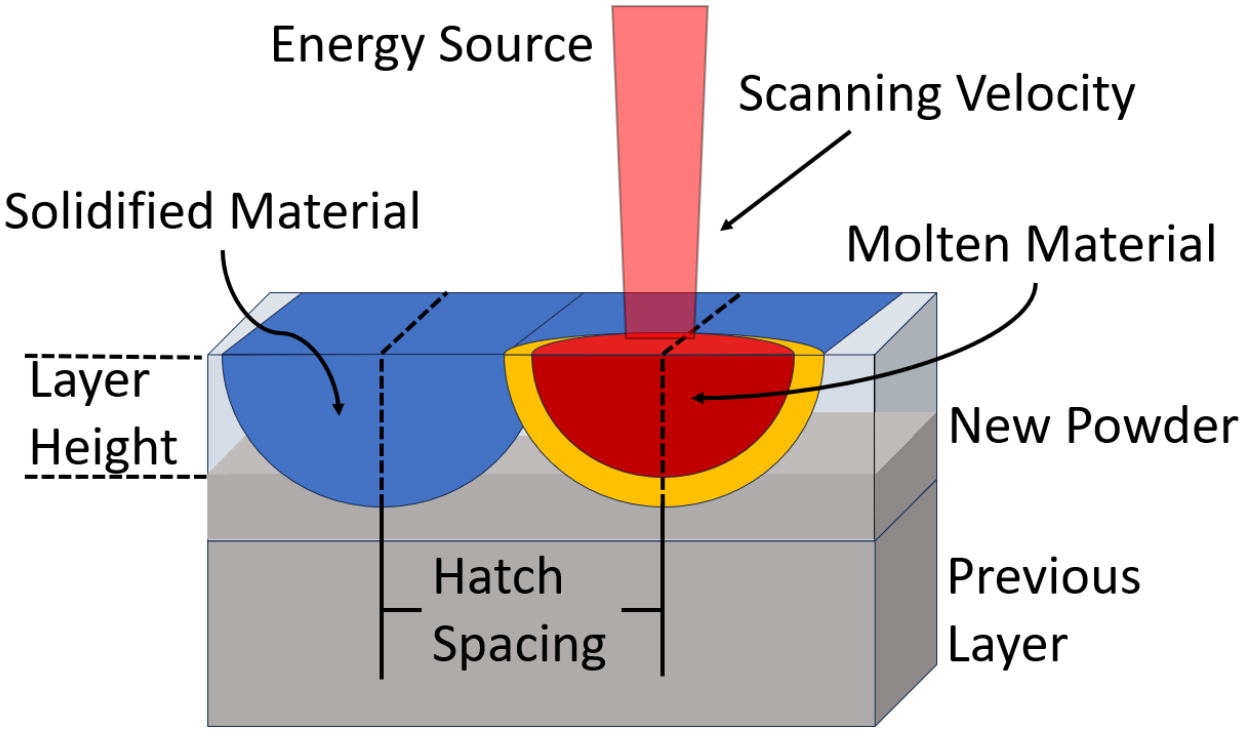

Figure 2: Generalized Melt Pool

While SLM utilizes complete melting, SLS bonds particles together more superficially. The surfaces of the particle fuse together without completely melting at elevated temperatures. This Solid State Sintering (SSS) process is driven by several reactions, but are primarily dominated by diffusion [26]. Semicrystalline structures, such as nylon, may be used individually while other materials may have their particles coated in a binding agent to facilitate the sintering process [5],[27]. An example of the binding process in SLS is depicted below in *Figure 3.* Particles are heated which causes necking between adjacent spheres. With enough thermal energy the neck expands and reduces the total porosity captured between particles.

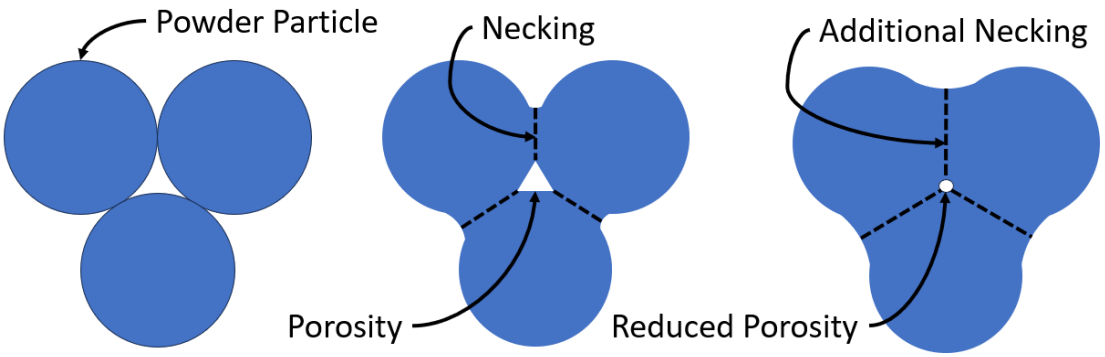

Figure 3: Selective Laser Sintering Powder Binding [1],[22],[26],[27]

The type of material strongly impacts the amount of energy that can be absorbed into the powder, mandating that materials and processes are thoroughly tested before entering production. Powder materials tend to absorb more energy than their bulk counterparts [28],[29]. SLM is strongly impacted by the particle size and distribution of the selected powder. Mixtures of coarse and fine powders (within a range) tend positively impact the density of completed parts while using only coarse or fine powder increases the likelihood for generating failure modes. The shape and size distribution of these powders play a key role in SLM. The percentage theoretical density, ultimate tensile strength and hardness of atomized powders increased with greater energy densities [23]. While gas-atomized particles present superior densification and mechanical properties at low energy densities, the percentage theoretical density and mechanical properties in water-atomized powders were comparable to their gas counterparts with high energy densities. Having a more spherical powder produces better flowability and better particle packing; allowing for the creation of dense powder beds and producing parts with greater surface finish, dimensional accuracy, and density compared to less spherical powders. Using powder that has a more prevalent quantity of fine particles negatively affects these properties due to increased friction [30],[31].

As metal materials are the building medium for SLM, the amount of energy that they may absorb from photons is essential in creating their processing parameters. Light from lasers, especially light generated in the long wavelength band where photon energy is low, is mostly reflected except for a small portion which is absorbed. A portion of the energy is absorbed by the bound electrons, excitons, lattice vibrations, and other oscillators in the powder [19]. Using the Fresnel equations, which describe the reflection and transmission of light when applied to a media, the absorptivity of the S and P polarizations can be determined; where S polarization is light that is transmitted parallel to the plane of incidence (reflected) and P polarization is light that is transmitted perpendicular to the plane of incidence (absorbed) [32]:

$$R_s = 1 - \left| \frac{cos\theta - (n^2 - \sin^2\theta)^{\frac{1}{2}}}{cos\theta + (n^2 - \sin^2\theta)^{\frac{1}{2}}} \right| \qquad (3)$$

$$R_p = 1 - \left| \frac{n^2 cos\theta - (n^2 - \sin^2\theta)^{\frac{1}{2}}}{n^2 cos\theta + (n^2 - \sin^2\theta)^{\frac{1}{2}}} \right| \qquad (4)$$

Where R_s is the reflectance or the amount of power reflected from the surface, and R_P the transmittance, or the refracted portion that is transmitted to the medium. The variable n is the complex refractive index of the material [32]. Subsequently, irradiance or transmitted power can be determined by using conservation of energy [33]:

$$T_S = 1 - R_S \quad (5)$$

$$T_P = 1 - R_P \quad (6)$$

These laser parameters and their interactions with the selected powder are critical to the success of a PBF print. By understanding the amount of energy reaching the powder layer, the v and h (D in one dimension) can be addressed from equations (1) and (2). These parameters are

driven by the scanning strategy implemented by the printing machine or the desired part outcome. The length, direction, and distribution of scanning lines all effect the thermal energy at each point in the part. Contour offset scanning, partition scanning, spiral line-filling scanning, and other scanning strategies all hope to control this gradient for desired internal stresses and warping [34], [35], [36]. To reduce residual stresses strategies such as profile scanning, which generates spiraling paths that shift inwards along the boundary of layer slices, are implemented. This type of strategy serves to constantly change the direction of the laser path to minimize internal stresses [37] . For large parts or thin-walled structures, large scanning vectors can cause increased warping, so other novel methods and scanning strategies have been proposed to combat part defects [38],[39].

Scan strategies can have a massive influence on the internal stresses generated in SLM. Scanning is often broken into two separate scanning modes, contouring and filling. This is done to increase the surface quality and dimensional accuracy of parts along their edges. The internal section is then filled using one of many scanning patterns [1]. Because the scanning strategy impacts the thermal history of the printed part at a local level, failures may occur in specifical points on a part that have seen unique thermal profiles in comparison to other locations on the build plate. This can manifest as thermal distortion, keyholing, balling or other failure modes [40]. Several scanning strategies are outlined below in *Figure 4*. Often multiple types of scanning strategies are implemented at the same time to sufficiently distribute the thermal concentrations within the part.

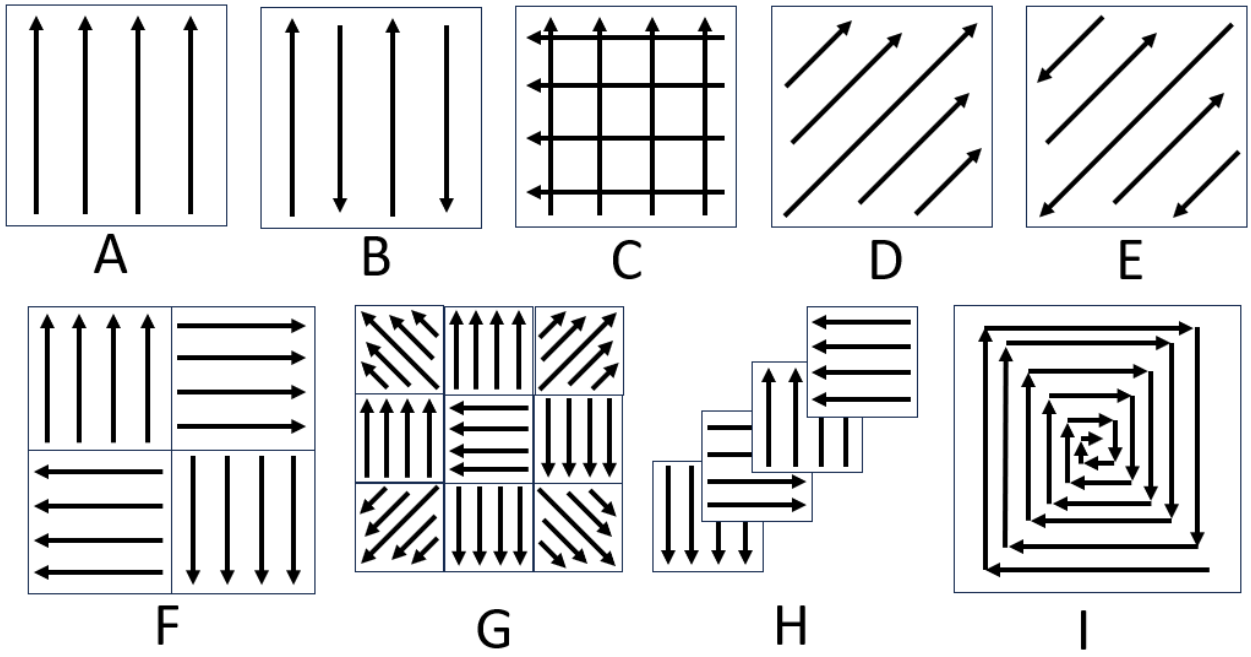

Figure 4: Selective Laser Sintering Powder Binding [41]

A) *Unidirectional* **B)** *Bi-directional* **C)** *Cross* **D** and **E)** *Variation of scanning sequence uni- and bi-directional* **F)** *Island scanning strategie* **G)** Alternative island scanning strategy **H)** *Uni-direcetional double pass 90°* **I)** *Modified helix*

Each of these scanning methods impacts the microstructure of the printed layer and affects the underlying substrate as well. The exact effects on the microstructure of the printed part are dependent on the material being printed and the type of scanning strategy used. One example of controlled grain structure is in Ti-64, where the direction of grain grown tend to be parallel to the laser path [42]. While grain structure may vary from material to material, there are scanning practices that regularly improve print performance such as using island printing or alternating layer print directions. Longer scan vectors and larger scanning islands exhibit reduced porosity and produce parts with fewer defects, however these do not necessarily coincide with optimal mechanical properties. There exists a range of scanning vector length when balancing the different parameters of the scanning strategy. [43]. Printing components with a

unidirectional scanning path result in weaker parts than those printed with raster rotations between layers [43],[44],[45].

Combining characteristics of the material powder, the selected scanning strategy, and the energy output of the laser, bed or powder build temperatures should be considered to minimize the formation of defects. Frequently, SLM requires an inert environment to operate, normally by filling the build chamber with argon or nitrogen gas. This is done to prevent oxidization as the metal powders are rapidly heated and cooled during the scanning process and is an essential environment for many of the high-end materials that SLM is compatible with. The build chamber may also be subject to an elevated temperature to assist with the printing process [46]. The build begins by adding an initial layer, often of greater thickness than that of the normal layer thickness. The fiber laser then scans the layer several times to heat the build plate, the build plate is lowered, and a new layer of powder is added into which the part geometry is scanned onto [13], [47]. The layer thickness of each slice is often between 20 μm to 120 μm to balance part resolution, energy deposition characteristics, and powder flowability [46].

Originally, SLS and SLM machines were designed with CO_2 lasers, but have since moved to Nd:YAG (Neodymium-yttrium aluminum garnet) or Yb:YAG (Neodymium-yttrium aluminum garnet) fiber lasers. Newer lasers have shifted towards shorter wave lengths as the metal powder is more responsive to wavelengths in the infrared region. The laser speed, power, spacing, material absorbance, and layer thickness all interact together as common parameters to modify in the SLM process as they all modify the volumetric output energy density [13]. Failure to ensure that the energy density at each point in the printing process is within an acceptable range result in defects such as balling or keyholing. The heat capacity and latent heat are key characteristics to account for during the melting process and are heavily dependent on the layer

thickness and type of materials being melted. Low energy density scans, normally caused by insufficient laser power, fast scanning speeds, and thick layers result in balling during the printing process. This is caused when the material on the substrate binds with the melted particles on the top surface and does not merge with the material below. Balling can be mitigated by increasing these parameters to optimize the energy density, rescanning the part to promote wettability, or reducing the quantity of oxygen in the build chamber [48]. However, increasing the energy density too high can also result in material evaporation and keyhole phenomena [49]. This creates zones of ideal conditions that should be met. For example, incorrect hatch spacing can create keyholing if the melt lines are too closely connected, or they can create porosity if they do not fuse together properly. Finding the correct combination of laser power, scanning methodology, material, and bed conditions for the print is essential for successful SLS and SLM printing.

1.1.1.2 Electron Beam Melting

Electron beam melting shares many qualities with SLS and SLM, except that it utilizes an electron beam instead of a photon laser as its method of energy delivery. First commercialized in 1997 by Arcam AB Corporation in Sweden, Arcam has been the only company selling EBM machinery until General Electric acquired the company in 2016. Competing EBM machines and research machines have struggled to produce comparable results [50] [51] [52] [53]. Unlike printing methods that utilize infill to reduce material costs, such as FDM, EBM produces high density metal parts, like that of SLM. These two printing methods leverage the same fundamental principle of PBF, but both present large differences in practice. This is due to the nature of energy transmission of electrons and photons. However, the primary mechanics are

similar; a heat source selectively passes over a bed of powder to melt particles layer-by-layer [54] [55].

One of the specific advantages of using electrons as an energy source is the ability to move an electron beam very quickly through electromagnetic lenses. While SLS and SLM require a lens to manipulate the position of the laser, this process is inertia-free when using EBM, allowing the beam to travel up to 100 km/s. This allows for rapid melting across the build chamber and for the implementation of unique cooling techniques. This benefit comes at the cost of requiring vacuum conditions for operation, unstable processes caused by charged materials, and the limitation of EBM to conductive materials [54].

An EBM printer has a similar housing as other PBF methods; namely powder magazines or hoppers, a recoater, a build chamber, and an energy source. CAD data is fed to a slicer which breaks it into layers that can be interpreted as printing operations by the machine at each layer. The housings are prepared by filling them with atomized powder and the build chamber is placed under a vacuum of 10^{-4} – 10^{-5} millibar. A controlled supply of a light gas such as helium is provided to at ~10^{-3} millibar to prevent powder from becoming charged and failing the print [50], [51]. Using a heated tungsten filament or a lanthanium hexaboride cathode, electrons are accelerated, focused, and deflected with electromagnetic lenses, reaching a maximum beam power of nearly 3 kW. The two types of emitting mediums produce different effects. The tungsten filament will produce a larger beam for power exceeding 1 kW, the lanthanium hexaboride beam has a consistent beam diameter up to 3 kW. This precision comes at the expense of increased sensitivity to failure with most materials. Upon the completion of the final layer, the chamber is often filled with helium and left to cool before the part is removed [54].

Powder is introduced to the printing area similarly to SLM; using scrapers to deposit thin layers of a specified material. This can be done with hoppers, or with the assistance of vibrating chambers, but the basic principle is still followed [53]. The thickness of these layers is selected based on the characteristics of the properties desired in the final part, namely the part's layer thickness. The build plate is initially pre-heated and is normally a similar or the same material as that of the powder. Normally, spherical gas atomized powders are used with particle sizes ranging from 40-105 micron. Particles much smaller than this range result in process instabilities, but larger particle sizes can be used at the expense of flowability in the powder [54].

The applied powder is heated by the build chamber ambient temperature and again by running the electron beam over the surface several times. This initial step provides the necessary thermal energy in the building volume to maintain temperature and sinters the powder together. The electron beam scans the surface several times with increasing power up to ~3 kW. Strategies and printing temperatures are material, powder size, and process dependent, but have ranges from 300-1100 ℃. Unlike laser ambient PBF techniques, the high build chamber temperature results in modified microstructures and internal stresses throughout the whole part [56], [57]. Since the laser-based systems often occur at much lower temperatures, the grain sizes of these AM techniques tend to be much smaller than the course grains produced in EBM [58].

Again, the primary difference between EBM is the medium in which the energy is delivered to the powder bed, which results in critical differences between the two methods it and the other PBF methods. In SLM, photons deliver energy close to the surface, on the order of nanometers. Electrons provide energy on the order of micrometers and require the use of vacuum environments to limit obstruction of the electron beam. For EBM, energy delivery ends up being

a function of the electron energy, the atomic number of the material in question, and the impact angle [59]. To achieve 100% density in parts and prevent failure points, the melt pool must be 3-4 layer thicknesses below the surface [60]. Following best practices and tuning parameters result in 99.5% or greater density, but it is still not uncommon to find defects of trapped gas bubbles in printed parts [61], [62]. Modifying the process parameters also strongly impacts the grain structure of the part with effects such as grain coarseness, isotropy, and homogeny of chemical composition [54], [63]. While a variety of materials have been studied for use with EBM, the applications are limited to metals with high conductivity, as the conductive nature is a requirement of the EBM process. This has resulted in most of the existing knowledge of technology being relatively limited with a focus on alloys.

1.2 Objectives for SAML

In the last several years, the University of Oklahoma has expanded its efforts to support the United States Air Force through research surrounding additive manufacturing. After securing several grants, the Sooner Additive Manufacturing Laboratory (SAML) was created to better develop additive manufacturing capabilities in the state. The SAML emphasizes operationalizing additive manufacturing with respect to airworthy components with a wholistic process that includes reverse engineering, design for AM, process and quality control of AM, post processing, and part characterization. Key focuses include integration of machine learning, in situ monitoring, and reduction in required critical data capture. Two of the driving projects that the SAML was tasked with revolve around the operation and testing of the General Electric (GE) Concept Laser M2 Series 5. One of these projects is to provide data on additively manufactured Ti-64 (90% titanium, 6% aluminum, 4% vanadium by weight) per the GE specifications.

1.3 Thesis Outline and Motivations

This thesis is intended to provide an overview of PBF processes, the manufacturing practices and processes being implemented at the SAML for tensile testing, and to present a preliminary study over the capabilities of the GE Ti-64 printer to guide decision-making on the overarching Air Force Project. It will first go over the original printing strategy for the Air Force project and touch on progress, developments, and challenges that resulted in this study. Specifically, there is interest in reviewing failure modes and process improvements that have been made along the way. Touching on most avenues of the experimental process and working through hurdles in advance will serve to provide an improved roadmap for the remaining samples that must be tested and evaluated. Next, this work covers the preparation of specimens from cradle to grave alongside tooling and analysis that guided decision-making. As mentioned in **Section 1.1**, there are several steps to the 3D printing process and several additional steps to prepare specimens for testing and analysis. Each of these steps are critical as they can impact outcomes of the experiment and outline areas that may require additional care moving forward to maximize efficiency. Material testing and procedures will be discussed in **Chapter 4**, with data processing and analysis occurring in **Chapter 5**. **Chapter 6** will present concluding remarks and make recommendations that future processes can build on.

Chapter 2: Modified Study and Process Considerations

2.1 Printing Setup

One of the requirements for the Air Force grant is to utilize the GE provided parameters while using their machines. This is done to provide a level of process control while using the AM technology. While locking the parameters down provides the necessary control to test the GE system, this has presented several challenges when attempting to print parts using the machine. Nowhere has this been more prevalent than with the use of the steel recoater blade. Since the printing parameters must stay constant, this limits the amount of control that can be exerted over the printing process.

The print in question was sliced with contour parameters of 0.095 mm CAD offset, 210 W laser power, 825 mm/s laser speed, a 75 μm spot size, and a minimum vector length of 0.03 mm. The internal portion of parts was sliced with slightly different parameters as surface quality is being addressed with the aforementioned parameters. The bulk material is sliced with a 0.11 mm CAD offset, 370 W laser power, 1700 mm/s laser speed, a 115 μm spot size, and no minimum vector length. Laser scanning is completed using a bidirectional island scanning strategy that is initially printed at 135° and is rotated by 67° between subsequent layers. Each island is sliced to be 15 mm wide and shifted by 1 mm each layer. Layer height is 60 μm per the GE Balanced 114 parameter. Slicing is completed using GE's in-house software with add-ins.

While control may be limited, the Ti-64 printer has functionally produced several rounds of prints over the last several months. After filling the powder chamber with virgin powder, the printing environment was purged using argon gas. With a positive track record, the first print to

create parts for the Air Force began using the above-mentioned parameters and a steel recoater. After over 100 successful layers, the steel recoater crashed into the part failing the print [64].

2.2 Print Failure

Thermal analysis showed that both the build plate and the built part had expanded beyond the layer height of the recoater (~60 μm for the Balanced Parameter 114). This was caused by thermal stresses being introduced into the build plate, creating residual stresses in both the parts and plate that caused the edges of the plate to rise up with a similar phenomenon being introduced into the printed specimens. Residual stresses are to be expected of a SLM print, but are not expected to be so extreme as to fail prints in their entirety. Measurements were taken of the printing plate using a DN Solutions SVM 4100 CNC and a Renishaw OMP60 probe along the parameter [65], [66]. This process is shown in Figure 5 below with the dimensional data displayed in Table 3. Since the build plate was warped, measurements in the Z-axis will be presented relative to the lowest measured point. The origin of the machining operation is centered about the build plate and point 1 is located in the bottom left corner of both images with points 2-6 proceeding in a clockwise direction around the parameter. The front and rear edges of the plate could not be accurately measured with the probing tool as the printed component did not leave enough remaining surface to clear the probe radius (3 mm).

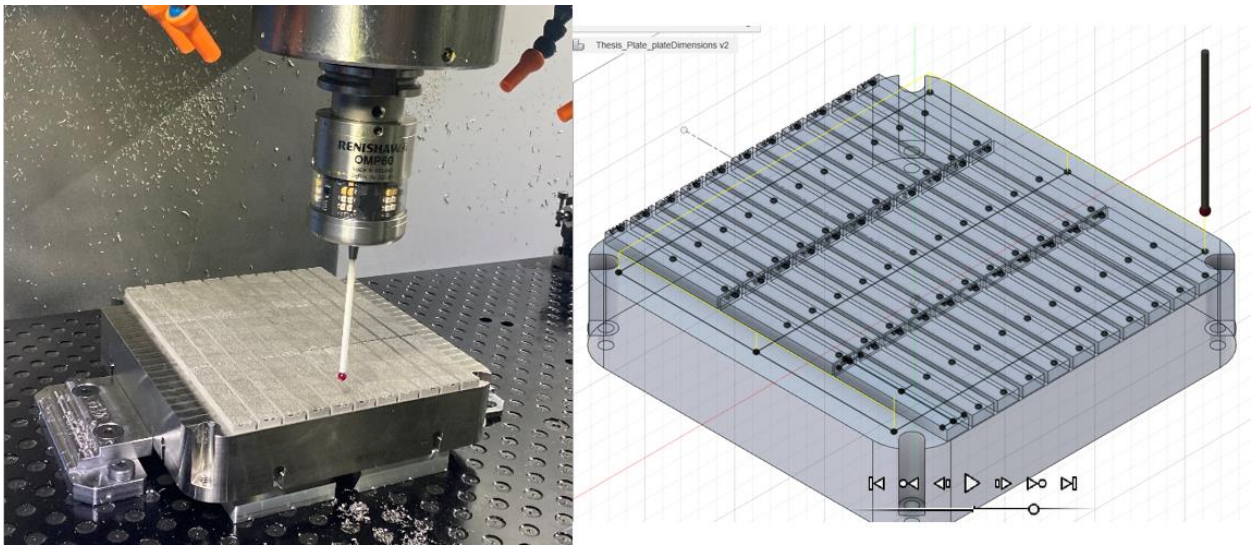

Figure 5: Build Plate with Partial Samples

Table 3: Dimensional Data of Warped Plate

Point Location	X (inches)	Y (inches)	Z (inches)
1	4.3326	3.8228	0.0079
2	4.3227	-0.001	0
3	4.3232	-3.8228	0.0023
4	-4.323	-3.8225	0.0047
5	-4.3328	0.0008	0.0019
6	-4.3227	3.8232	0.0101

When comparing the lowest point to the highest point along the parameter we see a maximum Z-height of 0.0101 in (256.54 μm). The original build plate was machine to be flat in the same measuring vice to $\pm$0.001 in or tighter. This indicated large fluctuations in the entire build plate from a single print. A similar study was conducted for the samples welded to the build plate but discerning the difference between faults created by the crashed recoater, resulting stress warping, and tolerance stack up render the data limitedly useful. However, it was determined that the thickness of material that had completed printing exceeded 0.275 in and, with the trend of unsuccessful prints using the steel recoater, may provide limited data about the effects of the recoater blade.

2.3 Salvage Sample Selection and Experiment Design

With the partially completed print and continued complications using the steel recoater blade, the build was determined to be a valuable tool to evaluate the performance of the GE SLM system and begin stress testing specimen preparation and evaluation. The build plate was composed of 33 potential samples which were broken into 5 subcategories to generate the maximum amount of data going forward. These categories can be seen below in *Figure 6*. GE specifies several different heat treatment methods and provides material data for the printed parts and includes the properties for each of the heat treatments as well.

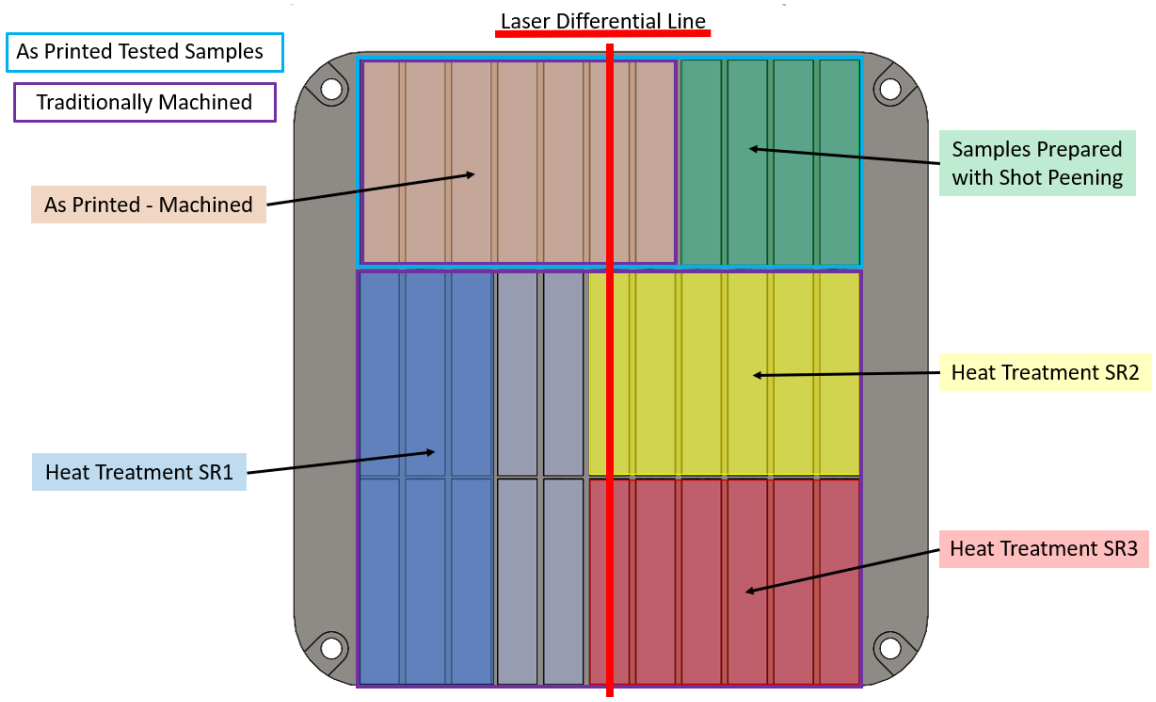

Figure 6: Build Regions with Descriptions

These regions were selected based on the dual laser zone and how Heat Treatment Stress Relief 1 (SR1) Stress Relief 2 (SR2), Heat Treatment Stress Relief 3 (SR3), and the as printed (SR0) characteristics reacted with exposure to the dual laser zone manufacturing (denoted by the

red line). The GE SLM machine is equipped with two lasers that work in conjunction to expedite the production of parts. The zone that separates the two lasers, denoted as the differential line, may produce parts with distinctive characteristics that should be understood. The regional separation is intended to provide one of the experienced SAML microscopists with a portion of each sample to analyze any differences in microstructure, hardness, or other parameters while evaluating the range of GE's provided specifications. Stress Relief 1 (SR1) and Stress Relief 0 with Shot Peening (SR0 Shot Peen), were included in the test to gather additional data. Within these regions, samples were given specimen numbers as shown in *Figure 7*.

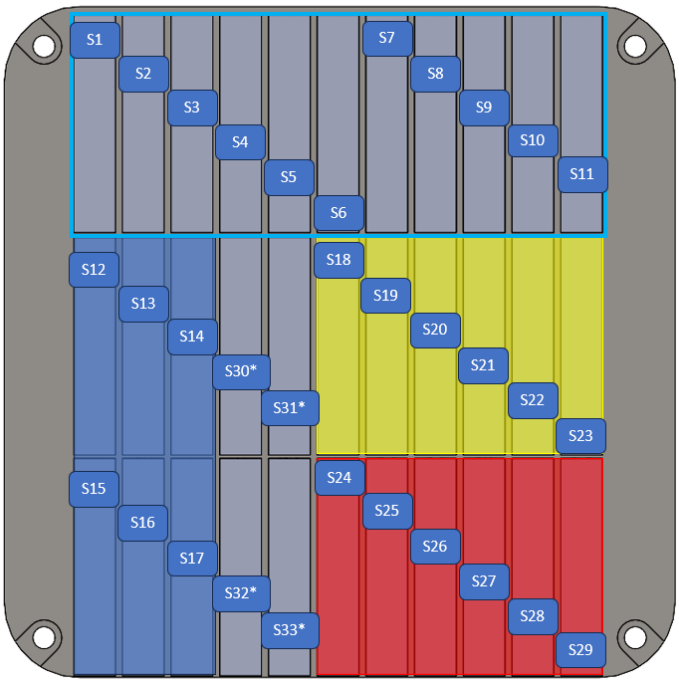

Figure 7: Build Regions with Sample Numbers

Samples 30*-33* were kept in reserve to provide additional data if a set of samples were improperly treated and for future microscopy projects. The four primary regions are based on the GE stress relief specifications SR1, SR2, SR3, and the as printed components SR0. The addition of the green zone for shot peening was determined after a project involving fatigue life presented

itself to the lab. Originally, specimens were to achieve a build height of several inches to manufacture a series of ASTM E8 round S3 specimens which were to be no less than 0.5 in in diameter. An image of the full scale CAD model is presented in *Figure 8* below.

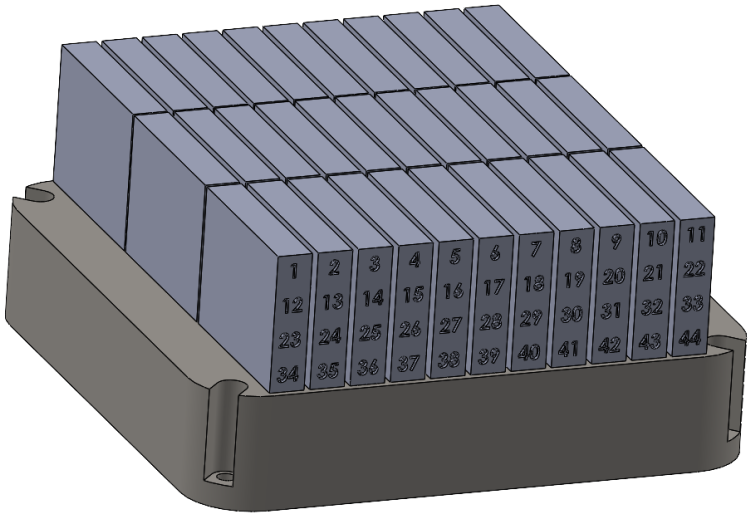

Figure 8: Intended Build Plate

Since the maximum height did not permit the use of a standardized ASTM E8 sample, an alternative specimen type that could be manufactured was selected [67]. A specimen that is compatible with available testing equipment and coincides with the dimensions of the available stock was selected, ASTM D638 Type V [68]. The thin stock mandated the use of a relatively small specimen that does not exceed the 50 kN load cell limit of the Universal Testing Machine and is compatible with DIC sample macros for data analysis [69] [70]. A drawing of the ASTM D638 Type V specimen is outlined below in *Figure 9*.

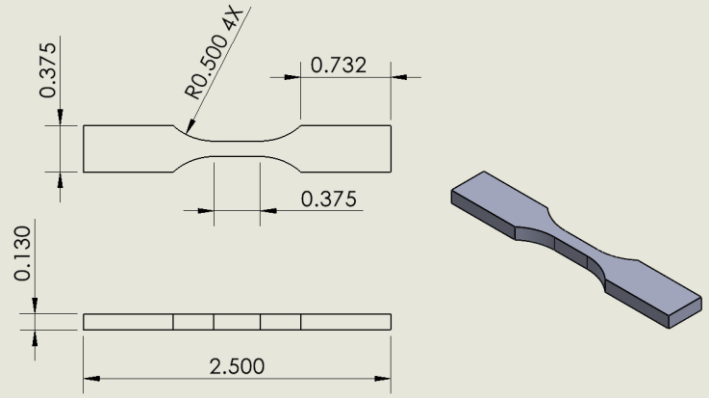

Figure 9: CAD Drawing for ASTM D638 Type V

2.4 Thermal Stress Relief

With a melting point near 1660°C or higher, titanium has found many uses in aerospace applications as a high-strength low-weight material in low to moderate temperature regimes. Titanium has two primary phases, a body-centered cubic (bcc) array and close-packed hexagonal array. The bcc array, referred to as the beta phase, is normally only found at high temperatures or in alloys. The hexagonal array, referred to as the alpha phase, is more common as it is stable at normal conditions and in commercially pure titanium. Titanium is broken into 4 classes: alpha, near-alpha, alpha-beta, and beta which describe the presence of each phase in the material and the stability of the alloy. Ti-64 sits as a mixed alpha-beta structure that shares many of the benefits of the alpha structure alloys (heat creep strength, weldability) and beta structure alloys (heat-treatment response, short-time strength, fabrication capacity). Ti-64 sits more closely to alpha phase alloys than it does to metastable beta alloys and stable beta alloys, making it one of the most widely used titanium alloys across all industries. Increasing the presence of beta phase in the alloy increases its costs as heat treatments and stabilizing elements become more necessary. With the addition of alloying elements, aluminum and vanadium in the case of Ti-64,

and heat treatment, beta phase is produced upon heating with alpha phase precipitating during the cooling process [71].

Ti-64 has temperature limitations that keep its operating conditions to roughly 400 °C with conventionally processed wrought/cast alloys achieving 595 °C. Treated materials can achieve higher operating conditions, but maintaining long term stability keeps the alloy to the temperature range. Higher temperature applications call for Ti-6Al-2Sn-4Zr-2Mo+Si or other alloys which are primarily used for turbine components, in sheet form for afterburners, and in elevated airframe applications. Alpha-beta phase alloys have compositions which completely transform into beta phase upon heating but revert back to alpha phase while retaining some beta phase after the cooling is complete. Transition from alpha to alpha-beta or entirely to beta is known as the beta transus temperature. This is the lowest equilibrium temperature at which the material is entirely beta phase. The beta transus temperature sits between 955 °C to 1065 °C with the temperature increasing as the percentage of Vanadium increases for alpha-beta phase titanium. Generally, a beta transus temperature of 1000 °C ±20 °C is considered for Ti-64, but specific suppliers will have slight variations in batches due to slight variations in chemical composition, namely oxygen content. This temperature is essential for most heat treatment processes as heat treatments of titanium normally involve bringing the material a specified temperature below, above, or at the transition temperature before subsequent processing. Heat treatment above ~427 °C must protect the alloy from ambient atmosphere. This is because the surface will react with atmospheric oxygen or nitrogen to form alpha cases. It also limits the formation of scale on the surface which requires removal. In the case of complications in the heat treatment process, Tables 8.8 and 8.9 in ASM: A Technical Guide offers oxide thickness

formation as a function of time and estimates on the minimum material removal after exposure to an oxidizing environment [71].

Stress relieving is the most common heat treatments given to titanium and its alloys because they can often be stress relieved without adverse effects to the strength or ductility of the material. Stress relief decreases the undesirable residual stresses that result from non-uniform hot forging deformation, nonuniform cold forming and straightening, asymmetric machining, welding and cooling of castings. In the case of SLM, this would directly correspond with laser path direction, layer-by-layer heat treatment, and welding of the printed part to the build plate. Stress reliefs assist with the maintenance of shape and helps alleviate losses in compressive yield strength. *Table 4* outlines each of the GE heat treatment procedures [71]:

Table 4: Comparison of GE SR to Traditional Ti-64 Heat Treatment [64], [71]

Treatment Type	Temperature (°C)	Time (h)	Cooling
GE SR1	900	1	Furnace Cool
GE SR2	840	2	Furnace Cool
GE SR3	730	2	Furnace Cool
ASM Solution Treating	955-970	1	Water
ASM Annealing	705-790	1-4	Air or Furnace
ASM SR	480-650	1-4	Air or Slow Cool

Annealing is used differently from producer to producer, resulting in a variety of heat treatments being described as annealing. Stress relief may be included in that annealing umbrella. In the case of the GE Ti-64 specification, this appears to be true as traditional stress relief occurs at temperatures far below that of the beta transus temperature and have little effect on controlling material microstructure. Common annealing treatments are considered mill annealing, duplex annealing, recrystallization annealing, and beta annealing. While callouts may indicate air or furnace cooling, these two procedures may result in different mechanical

properties as the cooling rates are different. With a beta transus range of ~1000C, recrystallization annealing is heating near the upper limits of the range, held for a time, and very slowly cooled. Annealing times are dependent on the thickness of the material and should be long enough to allow for complete transformation to the desired phase. Of the annealing processes, solution treating and aging produces some of the strongest characteristics in titanium. Solution treating brings the alpha-beta alloy very near that of the beta transus temperature and where it's held for a specified period. Solution treating normally involves quenching and aging to finalize the material specification. Generally, the higher temperature of the solution treatment, the stronger the resulting material. *Table 5* outlines this trend for a range of solution temperatures with air cooling and an aging treatment of 8 hours at 480 °C [71].

Table 5: Ti-64 Material Properties for Solution Treatment Temperatures [64], [71]

Treatment Temperature (°C)	Tensile Strength (MPa)	Yield Strength (MPa)
845	1025	980
870	1060	985
900	1095	995
925	1110	1000
940	1140	1055

The SR present by the GE specification is more closely related to annealing processes, specifically those of solution treatments for SR1 and SR2 and annealing for SR3. The intent of the different treatments is to modify the microstructure of the material to provide desired material properties instead of simply removing internal stresses as are normally associated with lower temperature stress relief processes. Unlike many common annealing processes, GE does not call for quenching or aging after the treatment process. Instead, it calls for furnace cooling in an argon environment. Since the cooling procedure is essential to the resulting material properties, appropriate heat distribution and thermal uniformity is essential in the furnace [64].

Thermal uniformity during heating is essential to meet specifications for the Air Force and the cooling uniformity of parts is also critical to ensuring components are not deformed. Thermal processing equipment must meet the standards of Aerospace Material Specification AMS2750 per SAE international. This document outlines the requirements for equipment used to process metals and covers a broad range of topics from sensor and processing requirements for a range of temperature profiles to outlines for thermal uniformity studies. Effectively, AMS2750 serves to certify, classify, and calibrate the performance of any processing furnace used to treat metal materials. Included in the purchase of the GE M2 Concept Laser was a Nabertherm Chamber Furnace N 41/H including a box with protective gas connections [72]. The protective box uses a type R thermocouple to regulate temperature in the furnace and provide data over the treatment of materials [73].

Adhering to AMS2750, the furnace is to be certified with calibrated thermocouples per ASTM E207 or ASTM E220 that sufficiently cover the temperature profile that the furnace will be operated at. Additionally, the furnace must undergo a Temperature Uniformity Study (TUS) and System Accuracy Tests (SAT) at regular intervals to garner a furnace classification and qualification. The N 87/H furnace is advertised to maintain temperature uniformity up to ± 10 °C giving it the distinction of Furnace Class 4 per AMS2750. However, the SAT and TUS must also be conducted to ensure the functionality of the equipment and regular calibration tests. To achieve these requirements, a thermocouple system capable of exceeding the minimum number of TUS sensors (5 sensor for a 3 ft^3 furnace) was designed (8 thermocouples and an additional ambient temperature sensor). Sensors include a SparkFun RedBoard Artimis Nano, SparkFun High Precision Temperature Sensor – TMP117, and 8 SparkFun Qwiic Thermocouple Amplifiers – MCP9600 [74], [75], [76]. Housing and components are shown below in *Figure 10*.

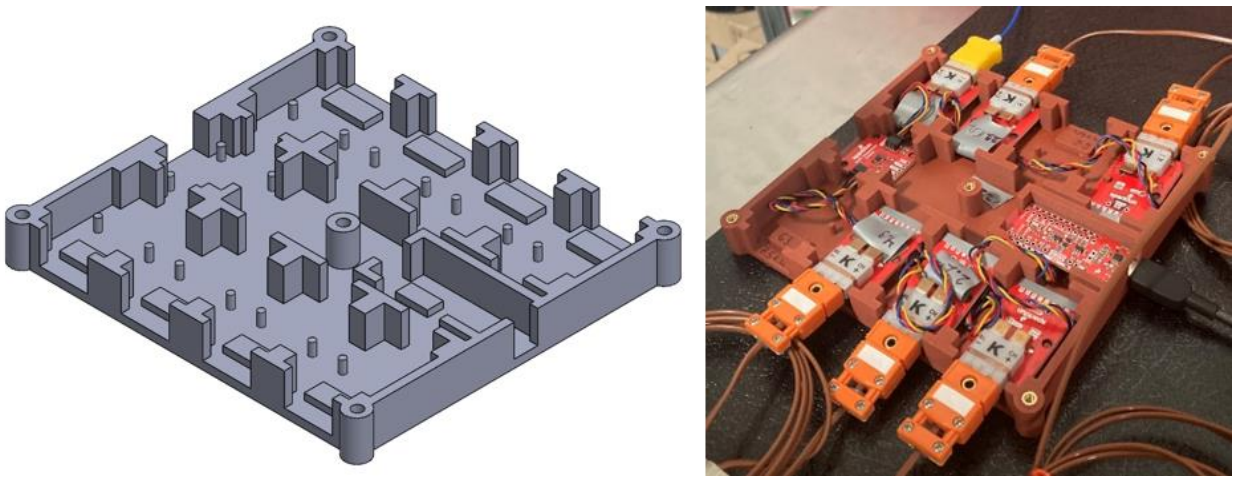

Figure 10: CAD of Thermocouple Housing and Completed Housing

Additional sensors are added through the SparkFun Qwiic connector system and provided different registry numbers by incorporating various sizes of resistors across the ADDR connector. Thermocouple adapters were purchased to ensure compatibility with the N-Type thermocouples. Initialization and troubleshooting of each sensor was completed by utilizing built in SparkFun libraries and made compatible with a MatLab script to output thermocouple history. Site acceptance testing and the thermal uniformity study are scheduled to occur after the completion of this study.

2.5 Microscopy and Polishing

Macroscopic capabilities are driven my microscopic structures and so the ability to observe grain structure proves to be a useful analytic capability in metallurgy. Processing Ti-64 for microscopy regularly involves electropolishing, chemical-mechanical polishing or electromechanical polishing, but results can be achieved using mechanical polishing alone [77] [78]. Microscopic analysis is limited in this study as several members of the SAML team excel with microscopy and analysis has delegated amongst the members. However, the preparation of

specimens exclusively using mechanical methods as preparation for optical and Scanning Electron Microscopy (SEM) are explored with resulting image quality used as a metric for polishing efficacy. The exclusive mechanical procedure is evaluated for several reasons. The simplicity of strictly polishing samples minimizes the number of parameters that need to be accounted for during preparation. The available and reliable methods of specimen preparation in both the SAML and at the University of Oklahoma's Samuel Roberts Noble Microscopy Laboratory (SRNML) primarily revolve around mechanical preparation and chemical etching.

Grinding equipment revolves around casting samples in some form of media, normally a polishing resin, and removing material with a range of abrasive particles to achieve increasingly planar surfaces. This could involve the use of grinding equipment such as automatic grinding machines, as illustrated in *Figure 11*, or belt grinders to increase the productivity of the process. While belt grinders are primarily used for roughing passes, automatic grinder-polishers can be used for both initial roughing passes and final polishing. Normally, abrasive papers are used for early polishing steps while lapping is used for finishing passes. Lapping utilizes a carrier disk and polishing abrasive that rolls along the surface of the carrier disk. While abrasive may initially roll along the surface in lapping, they will eventually become embedded into the polishing cloth and begin removing material. This can be facilitated by proper technique with polishing tools and sufficient application of the polishing media. Abrasive are normally composed of diamond, aluminum oxide, and amorphous silicon dioxide of varying sizes. Each size of particle damages the surface of sample, but also creates damage below the surface based upon the polishing procedure [79]. By progressively reducing the size of the polishing particle, the amount of subsurface damage is also reduced, producing better surface finishes [78], [80].

Figure 11: Struers LaboForce-3 Automatic Polisher

Previous polishing procedures abided by the following process: casting of samples in Allied 145-10010 EpoxyMount Resin at a 10:3 ratio with Allied 145-10015 EpoxyMount Hardener [81]. After being left to cure for 2 hours or greater, the part would be processed on a Struers LaboForce-3 polishing machine [82]. First with 220 grit sand paper, then with 9 μm glycol based polycrystalline diamond suspension, then with 6 μm diamond suspension water based, and finally with 0.05 μm FinalPrep alumina polishing solution de-agglomerated [83], [84], [85]. Each step was held for several minutes (~4) at 150-200 rpm. Samples prepared using this method are based on the Struers document “Metallographic Preparation of Titanium and Titanium Alloys” [78]. Samples prepared with this method have seen limited success and have resulted in the portion of this work dedicated to polishing procedures.

Chapter 3: Sample Preparation and Stock Characteristics

3.1 Part Removal

As mentioned in **Section 1.1** one of the critical requirements of the AM methodology is the removal of parts from the build area. In the case of SLM and most PBF, this is a more involved process than with other 3D printing methods. *Figure 1* illustrates the relationship between new powder layers and subsequent layers, including that of the build plate. In SLM the part is welded to the build plate and must be cut off, normally by means of Electrical Discharge Machining (EDM). Other methods may be used to remove parts from build plates, but they tend to result in less precise cuts which may damage parts or the build plate. With limited stock available on the build plate, a precise cut became necessary to maximize the titanium available for machining.

The EDM is one of the most critical tools at the SAML. Functioning similar to that of a water-jet, the EDM removes material by passing a moving wire along a 2-dimensional path within the operating area. The wire is charged to a specified voltage and frequency then submerged in a jet of treated water to create a dielectric barrier. As the wire passes near the cutting object, a spark just from the wire to the work piece, vaporizing a small portion of the material. Residual material from the process is washed away in the water jet into a drainage system. Parts that need to be removed are first mounted into the guide rails. This can be done through compression with the use of several screws and threaded workpieces that compress stock to the rails, or through the use of specialized tooling. In the case of printer build plates, a mounting plate was developed to attach build plates in the correct position and orientation to the EDM rails. After mounting the plate to the tool housing, the wire is adjusted manually and with

the machine interface. *Figure 12* illustrates the tilt motors that adjust the wire angle in relation to the Z-axis and the build plate mount. Normally, this angle is between 1-3° and is relatively easy to adjust with each motor tilting the wire within the respective x- or y- plane of the EDMMax 656W [86].

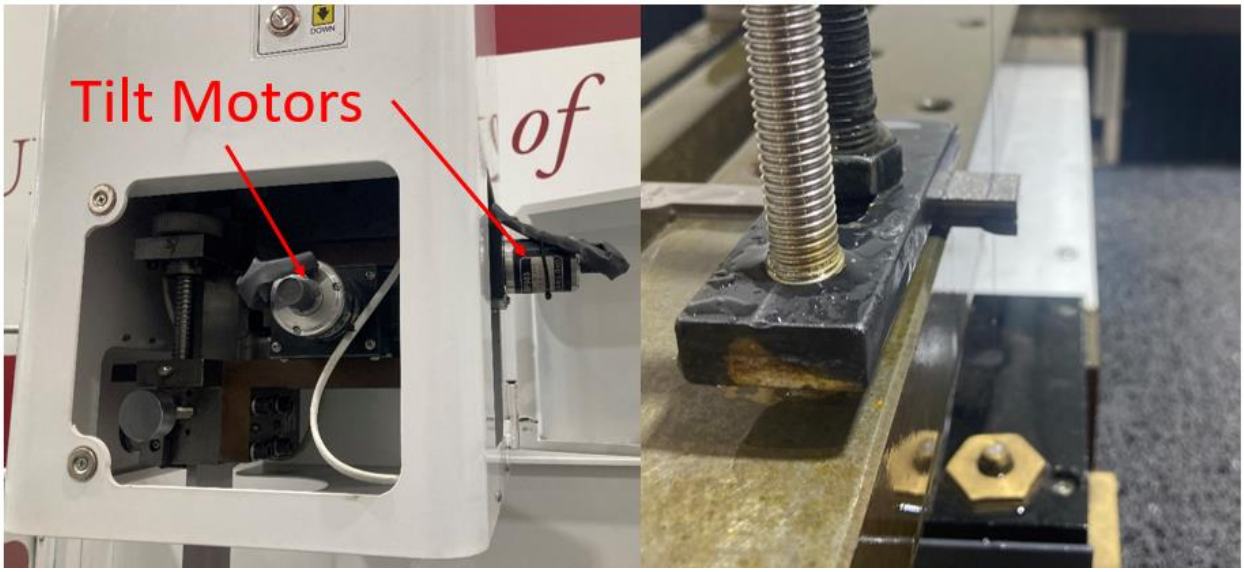

Figure 12: EDM Preparation

While the wire must be adjusted to the tilt of the angle of the build plate using stepper motors, the global x- y- positions must also be adjusted around the position of the build plate with the user interface. This is done by using the jog handle and using the built-in edge finder cycle, which detects when the wire interacts with an object. After edges have been found, the x- y- coordinates are set to 0. This position is considered the origin for any new cutting operation. Next, the cutting path is determined with a built-in geometry creation interface. The interface primarily uses simple shapes to create the desired cutting paths, but more complex shapes can be manufactured by importing drawings as .dxf files and importing them onto the machine. After setting up the cutting geometry, a wire offset, entrance point from origin, travel direction, and

final point are selected. The geometry is passed to the machine and a request to activate the water pump, wire, and high frequency voltage are presented. The frequency and voltage of the wire are impacted by several factors that must be set before the operation can begin. The thickness must be presented, in this case a thickness of 250-500 mm, along with the number of passes the wire will make, and the type of material being processed. Since the part is being removed, the number of cuts was set to 1, and the material is set to tungsten, which is processed the same as titanium in the EDMMax calculations. After activating all 3 of the constituents of the cutting process, the operation can begin. Over the course of several hours, the stock was removed from the build plate.

3.2 Specimen Stock Characteristics

Because the steel recoater crashed into the surface of the built part and a small layer of the build plates was removed with the specimen stock during EDM removal, the Z value of specimens remained inconsistent and could not be accurately measured. For subsequent evaluation, the height of each specimen stock is estimated to be 0.277 in. However, the x- and y-coordinates were captured using Mitutoyo AOS Absolute Digimatic Calipers [87]. Since the total quantity of data cannot be neatly represented in a chart, the minimum, maximum, average, and standard deviation are presented instead.

Table 6: Dimensional Data for Printed Stock

Parameter	Minimum	Maximum	Mean	Standard Dev.
Width (in)	0.6035	0.6085	0.60630303	0.00121193
CAD Width (in)	0.6			
Length (in)	3.1175	3.126	3.12021212	0.00229634
CAD Length(in)	3.125			

The dimensional accuracy of prints is quite high. While the width of prints appears to be consistently oversized, the inverse is true for the length of prints. This discrepancy may be caused by residual thermal stresses in the part. As mentioned previously, the print created enough distortion to warp the entire plate along the parameter. The printed components were also subject to these residual stresses and several of them had even removed themselves from the build plate along one edge (S3 – S11). This resulted in interest in estimating the residual stresses in the bars by determining the total deflection in each sample. These were analyzed using a Keyence VL-700 which can scan and render a model of each specimen [88]. *Figure 13* displays the model created with the scanner.

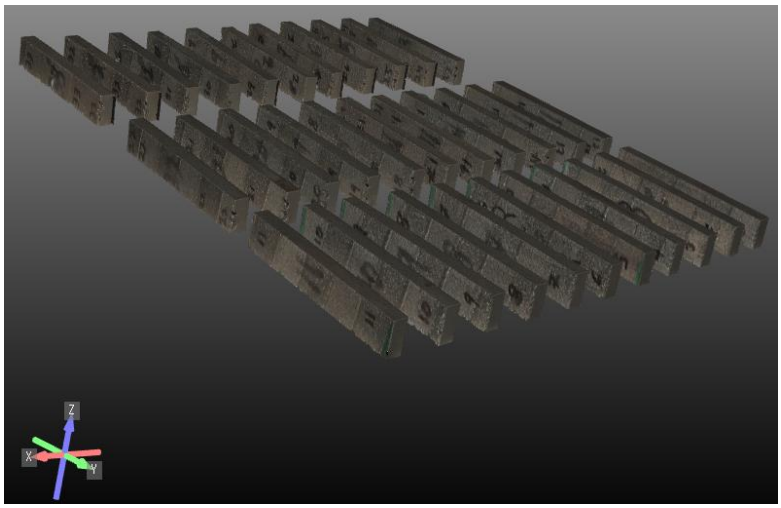

Figure 13: 3D Model of Samples

The samples were then divided into individual models which were evaluated by creating a plane along one edge of the specimen and treating the structure like a cantilever beam. *Figure 14* illustrates the process of selecting a small portion of face created by the EDM'ed surface. This side of the sample was selected because of the non-uniform shape of the printed face and because the EDM has very tight tolerance, leading to the assumption that the surface will best

indicate the deflection of the sample. This evaluation is completed with the aid of the 2-dimensional analysis tool in the Keyence software.

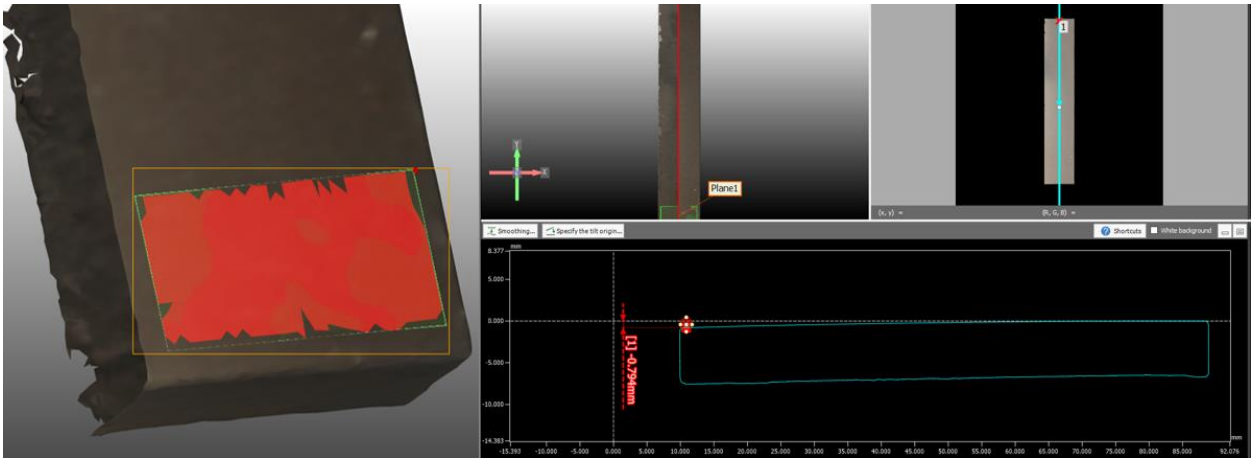

Figure 14: Deflection Analysis Using VL-700

The red text indicates the deflection value while the horizontal line is generated colinear parallel to the plane created to the left. The cross-sectional view is created by bisecting the surface along the red/blue lines in the upper-right. The residual stress is estimated by using standard deflection theory and evaluating the structure as a fixed cantilever beam using *Equations 4-8*.

$$\delta_{max} = \frac{FL^3}{3EI} \quad (4) \qquad F = \frac{3EI\delta}{L^3} \quad (5) \qquad \sigma_{max} = \frac{yM}{I} \quad (6) \qquad M = FL \quad (7)$$

$$\sigma = \frac{3Ey\delta}{L^2} \quad (8)$$

Where F is a point load, L is the beam length, E is Young's Modulus, I is the moment of inertia for a beam, δ is the deflection of the beam, and y is the distance between the neutral axis to the maxima. Several simplifications are made to perform the deflection analysis. First, the thickness of each bar is assumed to be 0.277 in. Second, the neutral axis is assumed to have the same deflection as the value derived from the VL-700. Third, the bar is assumed to have a

uniform cross-section and internal stresses along its length. Fourth, the GE-provided data for Young's Modulus is accurate for horizontal specimens of the Balance parameter. Finally, the measured length is assumed to be considered the maximum length of the bar. Solving for σ given these assumptions results in the minimum, maximum, mean, and median values in below.

Table 7: Dimensional Data for Printed Stock

Parameter	Minimum	Maximum	Mean	Median
Displacement (mm)	0.733	1.736	0.96672727	0.968
Stress (MPa)	139.1462017	353.557031	189.569568	186.7938096
Force (N)	222.3920177	567.959579	303.930617	299.5330984

The maximum value appears is specimen S16, which is in the lower left portion of *Figure 7*. Analysis will be presented in the results section **Chapter 5** and treats S16 as an outlier.

Before the printed stock was machined down, the surface roughness was also evaluated using a Mitutoyo Surftest SJ-210 surface roughness indicator. Three measurements were taken per specimen, two tests on the top surface and one on the side wall [89]. Tests were completed per *Figure 15* with the side wall test being evaluated in the y-axis direction as the thickness of the specimen did not permit evaluation in the z-axis. Three surface roughness parameters; R_a, R_q, and R_z were evaluated for each test. R_a is the arithmetic mean of the roughness profile within a measuring distance, R_q is the root mean square of the surface roughness, and R_z is the average magnitude of the five highest-profile peaks and valleys.

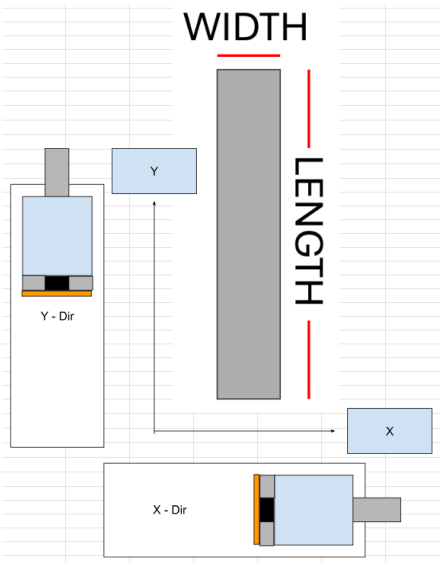

Figure 15: Deflection Analysis Using VL-700

Once again, the data is presented as the minimum, maximum, average, and standard deviation of the data in *Table 8*. GE data for surface roughness (R_a) is also presented.

Table 8: Surface Roughness of Sample Stock

Parameter	Min	Max	Average	Standard Dev.
Transverse R_q (μm)	10.827	17.645	13.467	1.4933
Transverse Ra (μm)	8.12	14.861	10.888	1.297
Transverse Rz (μm)	50.638	70.791	58.691	5.471
Longitudinal Rq (μm)	8.64	16.825	12.037	1.662
Longitudinal Ra (μm)	6.447	13.371	9.631	1.417
Longitudinal Rz (μm)	40.411	71.315	50.842	6.842
Side Wall Rq (μm)	7.86	14.837	9.865	1.464
Side Wall Ra (μm)	6.18	11.909	7.940	1.146
Side Wall Rz (μm)	34.91	60.045	44.452	5.890
GE Upskin Ra (μm)	-	-	18	-
GE Downskin Ra (μm)	-	-	10	-

3.3 Machining

Aluminum tooling was manufactured to effectively maintain tight tolerances while producing parts out of stock with predetermined dimensions. A 6” x 1.5” x 2” aluminum soft-jaw compatible with a machining vice was used as stock. A CAD model was designed in SolidWorks

and moved to Fusion 360 for Computer Aided Manufacturing (CAM). One side is a pocket that is designed to hold the raw titanium stock in place while the ASTM D638 Type V specimen has its perimeter machined as a contour. The other side is a slightly oversized female pocket to hold partially machined specimen for a final facing operation. The operations are shown below in *Figures 16 – 18.*

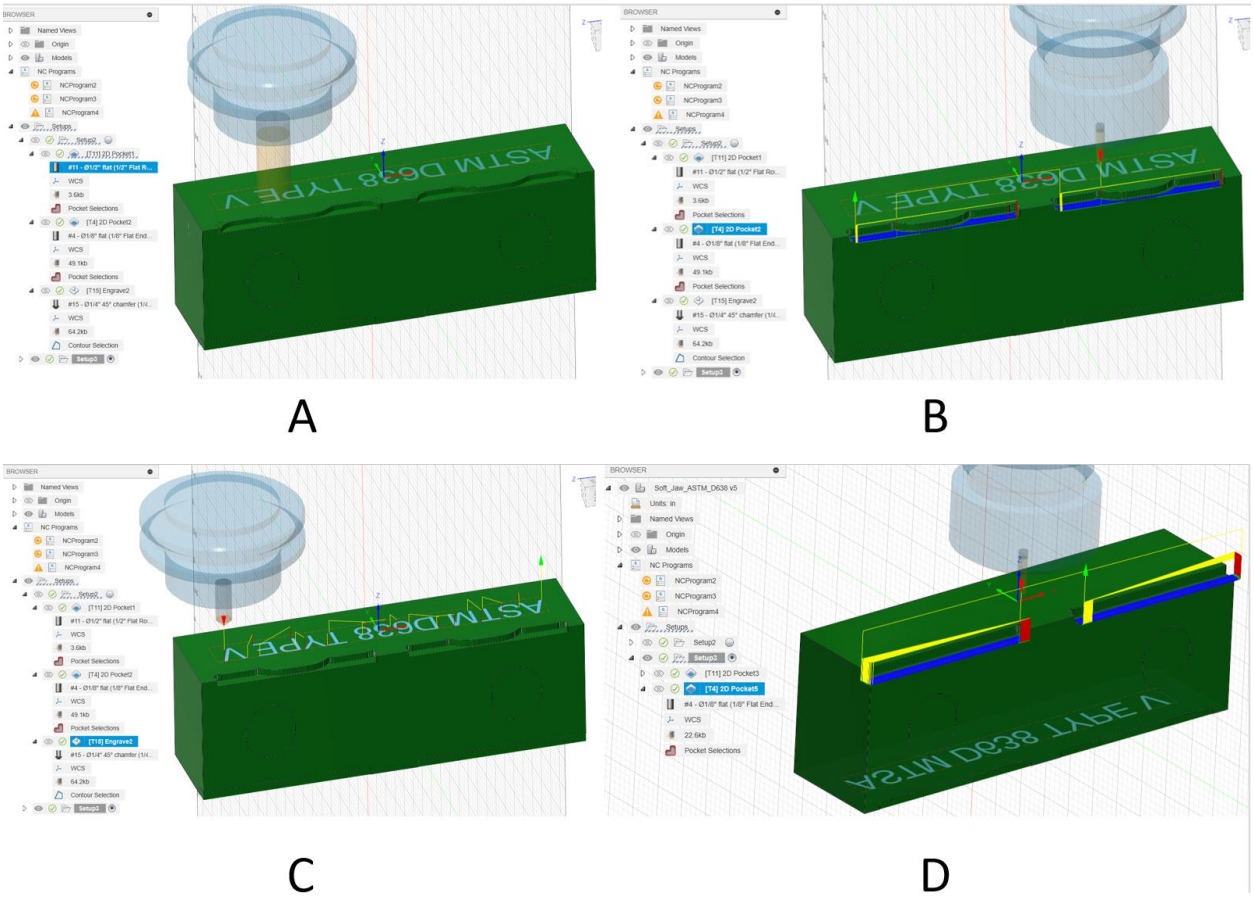

Figure 16: Machining Operations for ASTM D638 Type V Tooling

A) 1/2” flat roughing endmill 2D pocket operation. Spindle speed 5000 rpm, surface speed 654.5 ft/min, cutting feedrate 40 in/min, feed per tooth .0033 in, lead-in/out feedrate 40 in/min, with a maximum step-over of 0.1 in. **B)** 1/8” flat endmill 2D pocket. Spindle speed 12000 rpm, surface speed 392.7 ft/min, cutting feedrate 20 in/min, feed per tooth 0.00056 in, lead-in/out federate 10 in/min, maximum step-over 0.0125 in. **C)** 1/4” 45° chamfer engraving operation. Spindle speed 10000 rpm, surface speed 654.5 ft/min, cutting feed rate 10 in/min, feed per tooth 0.0005 in, lead-in/out 10 in/min. **D)** 1/8” flat endmill 2D pocket. Spindle speed 12000 rpm, 392.7 ft/min, 20 in/min, feed per tooth 0.00056 in lead-in/out 20 in/min. maximum stepover 0.0125 in.

The origin for the machining operation is set to be the center of the aluminum stock with stock values within Fusion 360 being set to align with the actual stock dimensions. This position was found using the built in “web” operation, which finds a midpoint between two edges, and the z-probe, which determines the vertical working offset. Operation feeds and speeds are generally determined by optimal load on the mill tool and derived using a machinist calculator, Fusion 360’s built in calculations, and the experience offered by Dr. Billings.

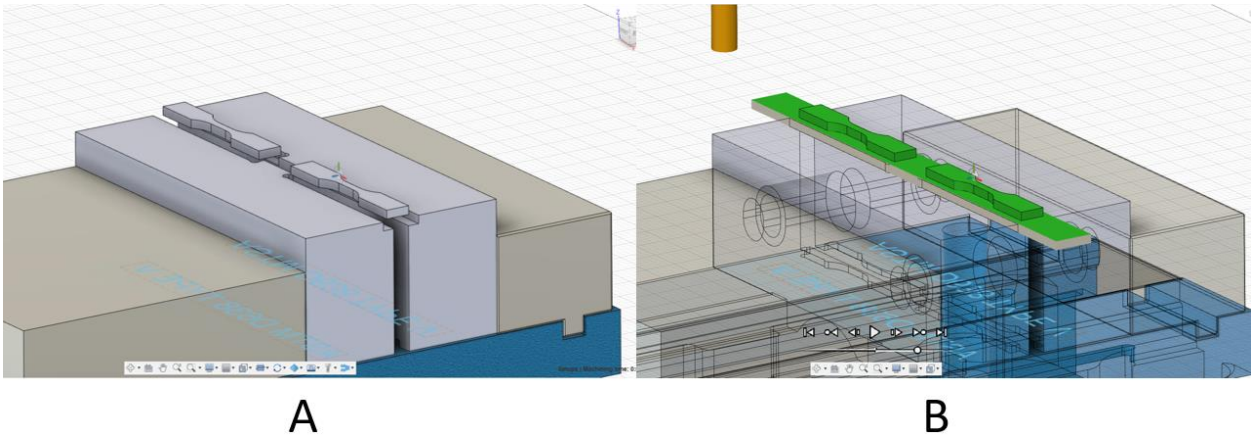

Figure 17: First Machining Operation for Ti-64 ASTM D638 Type V

A) Setup and positioning to develop tolerances for operation. B) C) 3/8” 6 flute flat carbide. adaptive clearing. Spindle speed 1833.45 rpm, surface speed 180 ft/min, cutting federate 20.9 in/min, feed per tooth 0.00273 in, lead-in/out federate 20.9 in/min, optimal load 0.0375, climb cutting.

Test specimens were machined using manufactured tooling as the origin. The back left corner of the jar was set to be the origin in Fusion 360 manufacturing. The assembly of the machining base, soft-jaws, and test specimens were arranged into a single assembly to accurately simulate the machining operation. Titanium stock dimensions were simplified as a single bar stock of the same length as the specimens total distance from end to end. By using the back soft-jaw as an origin point, simplifications like this became relatively mundane and allowed for multiple specimens to be processed without having to reset the zero point between machining operations because the tooling is stationary. For example, specimen, S1 and S2 could be placed

in the jaw, machined and removed, then replaced with samples S3 and S4. Operations only required replacing stock and restarting the necessary G-Code. After samples were machined on one side, the tooling was removed and flipped upside-down to expose the alternative tooling for the second operation. Remaining stock was removed using a facing operation and similar strategy. Unlike the first operation, the second operation sought to maintain a small portion of stock from each specimen. *Figures 18* C and *D* illustrate the remining stock.

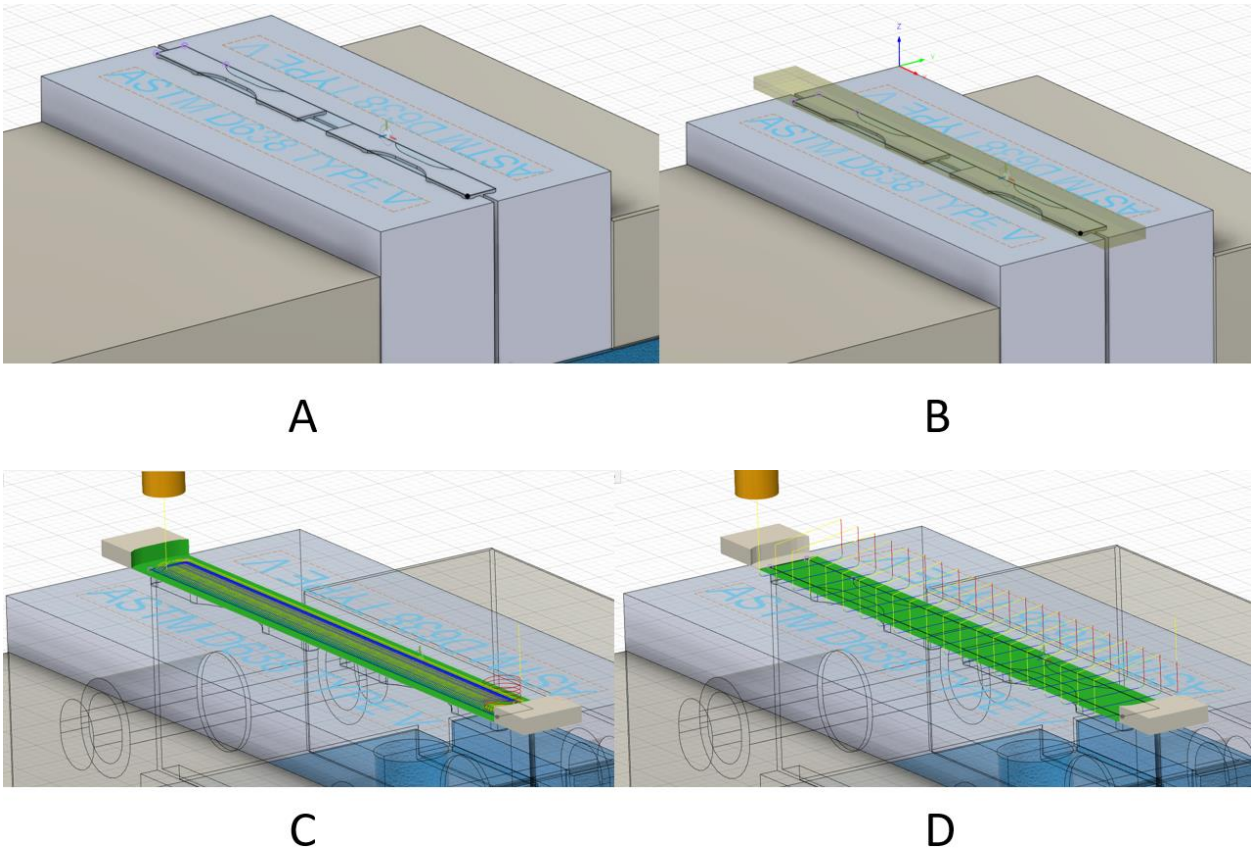

Figure 18: First Machining Operation for Ti-64 ASTM D638 Type V

A) Setup and positioning for tolerances. **B)** Stock design to guide machining operations and ensure tolerances. **C)** 3/8" 6 flute flat carbide. adaptive clearing. Spindle speed 1833.45 rpm, surface speed 180 ft/min, cutting federate 30 in/min, feed per tooth 0.00273 in, lead-in/out federate 30 in/min, optimal load 0.0375, climb cutting. **D)** 3/8" 6 flute flat carbide. Facing operation. Spindle speed 1833.45 rpm, surface speed 180 ft/min, cutting federate 15 in/min, feed per tooth 0.00136 in, lead-in/out federate 15 in/min, pass extension 0.1870 in, stepover 0.2625 in, climb cutting.

By refraining from milling down the stock on the edges, it would be maintained for polishing and microscopic analysis. These segments presented a pre-machine surface that is

relatively flat and sufficiently small, to fit into available polishing molds. While all samples were machined using the same tooling, samples that received heat treatment were machined after the treatment process to remove oxide formation and oxidized material.

3.4 Specimen Treatment

After processing, 5 different conditions were prepared for bulk material evaluation. Evaluating all 5 options permits an overview of the GE Balanced Parameter 114. The treatment designations were used to track the performance of each specimen while maintaining information surrounding their position on the build plate.

Table 9: Treatment Designations, Sample Numbers, and Quantity

Parameter	Treatment Designation	Specimen Numbers	Specimen Total
GE Stress Relief 0	SR0	1-7	7
GE Stress Relief 0 + Shot Peening	SR0shotpeen	8-11	4
GE Stress Relief 1	SR1	12-17	6
GE Stress Relief 2	SR2	18-23	6
GE Stress Relief 3	SR3	24-29	6

GE SR0 presents only printed samples. However, these components maintain residual stresses from the printing process and will deform upon machining, potentially bringing parts out of tolerance. As mentioned in **Section 2.4**, thermal treatments such as stress relieving can serve to minimize the effects of these internal forces. Since the treatment callouts are relatively vague, the SAML team used this study to evaluate and gain experience with heat treating before treating specimens for the Air Force. This resulted in 3 different argon infiltration strategies as all items that had been treated in the furnace to this point experienced oxidation. The GE SR1 not only serves to minimize the residual effects from printing, but also modifies the microstructure per the manufactures data sheet [64].

SR1 is indicated in *Table 4*, calling for bringing specimens up to 900 °C and holding the temperature for 1 hour. A Nabertherm Chamber Furnace N 41/H was set to complete this thermal treatment in 4 steps: Purge the chamber with argon at 20 SCFH at room temperature for 3 hours. Ramp from 30 – 900 °C at a rate of 900 °C/hour with an argon flow rate of 20 SCFH. Hold 900 °C for 1 hour with continued argon flow rate. Furnace cool with continued argon flow rate. The specification does not call for any specific rates. The furnace will not move on to the next step until the temperature conditions from the prior step is met. After ~24 hours the heat treatment was completed. The samples were not sufficiently protected by the argon gas and were oxidized, forming scale along the surface. Oxidized material was removed by CNC milling before testing. For SR2, a similar process was followed, but at a lower temperature, and without purging the chamber in advance. The Nabertherm furnace was set to complete the heat treatment in 3 phases: Ramp from 30 – 840 °C at a rate of 900 °C/hour with an argon flow rate of 5 SCFH. Hold 840 °C for 2 hours with continued argon flow rate. Furnace cool with continued argon flow rate. After ~24 hours the heat treatment was completed, and samples removed. SR3, received a combination of the first two treatments: Purge the chamber with argon at 10 SCFH for 3 hours. Ramp from 30 – 730 °C at a rate of 900 °C/hour with an argon flow rate of 10 SCFH. Hold 730 °C for 2 hours with continued argon flow rate. Furnace cool with continued argon flow rate. After ~24 hours the heat treatment was completed, and samples removed. A concise catalogue of the heat treatments is presented in *Table 10*.

Table 10: Expanded Heat Treatment Parameters

Process	Purge (h)	Temperature (°C)	Hold (h)	Argon Rate (SCFH)
SR0	-	-	-	-
SR1	3	900	1	20
SR2	-	840	2	5

SR3	3	730	2	10

The final treatment, shot peening, is not included in the GE specification. It is included to evaluate how effective surface treatments may be in combating residual stresses generated in "as printed" materials. Shot peening was implemented using 80 grit glass bead at 115 psi in the sand blasting cabinet. The pressure and grit are selected off available materials as a preliminary study to evaluate process performance. Velocity, and therefore kinetic energy, is evaluated based on conservation of mass and Bernoulli's principle assuming constant density. Shot coverage is a function of time as particle flow rate is held constant [90].

$$P_1 + \frac{1}{2}\rho V_1^2 = P_2 + \frac{1}{2}\rho V_2^2 \qquad (9) \qquad \rho V_1 A_1 = \rho V_2 A_2 \qquad (10)$$

$$V_1 = \frac{A_2}{A_1} V_2 \qquad (11)$$

$$P_2 - P_1 = \frac{1}{2}\rho \left(\frac{A_2}{A_1} V_2\right)^2 - \frac{1}{2}\rho V_2^2 \qquad (12)$$

$$V_2 = \sqrt{\frac{2(P_2 - P_1)}{\left(\frac{A_2^2}{A_1^2} - 1\right)\rho}} \qquad (13)$$

Where P_1 is compressor pressure, P_2 is atmospheric pressure, ρ is the density of air, V_1 is the velocity at the larger throat of the sand blaster, V_2 is the velocity at the exit of the sand blaster and is also considered the particle velocity, A_1 is the area of the larger throat of the sand blaster, and A_2 is the area of the exit. Making the aforementioned assumptions, V_2 can be found using Equation 13, ~1050 m/s. However, the exit velocity will be limited to the speed of sound (~343 m/s) as sand blaster is not equipped with a converging diverging nozzle. Samples 8-11 were treated using the same soft-jaws as shown in *Figure 19*.

Figure 19: Blasting Setup

Due to time constraints, Almen strips are not used to indicate surface coverage, so time relations are used instead. Shot peen coverage is estimated to be 100% with an exposure time of 4 minutes on each surface [90]. After machining and alternative processing, all specimens had their cross sections evaluated using Mitutoyo AOS Absolute Digimatic Calipers [87].

Tensile specimens completed preparation with the addition of a stochastic pattern applied using off the shelf matte or flat spray paint. Two thin layers of white primer are applied evenly to subjects and left to dry for 10-20 minutes. A fine layer of black paint is applied over the surface effectively speckling the entirety of the sample. If an excess of black paint is applied to the surface, a thin layer of white is applied after 10-20 minutes of drying. Surface pattern quality is evaluated using the Zeiss ARAMIS Adjustable Base and GOM Correlate Pro software [70].

3.5 Microscopy Preparation

Samples from each of the treatment profiles and duplicates for additional testing were cast in Allied 145-10010 EpoxyMount Resin and Allied 145-10015 EpoxyMount Hardener at a 10:3 ratio as shown in *Figure 20* [81]. Cast samples were then inserted into the Struers LaboForce-3 Automatic Polisher as shown in *Figure 11*. Samples were polished according to an improved polishing procedure outlined in *Table 11*.

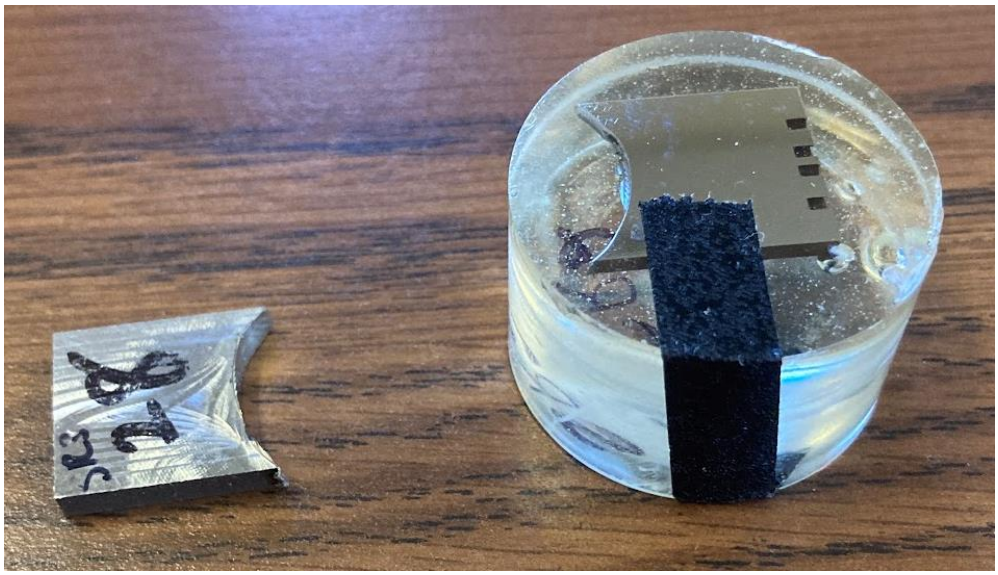

Figure 20: Epoxy Mounted Microscope Samples

Note that while polishing procedures can be optimized very well, especially for high end equipment, polishing is often considered an art. Technique, experience, and available equipment make the process variable. Polishing finishes may be off-set by modifications or improvements in a variety of avenues.

Table 11: Polishing Procedure

Particle Size (μm)	Rotation Rate (rpm)	Pressure (Struers Indicator Line)	Time (min)
220 Grit (~77.5)	150-300	2 - 3	~7
9	300	4	~7
6	300	3	~3
3	300	4	~3
1	300	3	~3
0.05	300 (150*)	3 (2*)	~5 (3*)
0.02	100	Hand Polish	~3

** Indicates a second operation with the same polishing wheel*

Particle sizes of 3 μm, 1 μm, and 0.02 μm were added to the previous polishing process in addition to the 220 grit sand paper, 9 μm, 6 μm, and 0.05 μm particles for the resulting polishing procedure outlined above [83], [84], [85], [91]. Additional samples were removed at each polishing step to illustrate the damage sustained by the Ti-64 surface.

Chapter 4: Sample Preparation and Stock Characteristics

4.1 Tensile Testing

Specimens were evaluated using an Instron 5969 Universal Testing System equipped with a 50 kN load cell and a Zeiss ARAMIS Adjustable Base Dual Image Correlation (DIC) system equipped with 75 mm Titanar lenses [69], [70]. The Universal Testing System was calibrated using a built-in calibration technique while the DIC was calibrated using a CP40/38/10588 object at a working distance of 684 mm. The cross head speed was selected to be 0.5 mm/min per Baufeld and Biest [92]. This value was compared against that of Foehring and was determined to be the more conservative of the two rates [93]. To ensure high quality DIC images and accurate data, samples were placed in the jaws using an alignment tool and a single image was captured using the DIC. The stationary image is subsequently processed to include an element along its surface. The pattern quality is then evaluated using a built-in function in the Correlate Pro suite. Alignment and surface pattern quality procedures are visualized in *Figure 21.* After a high-quality pattern is determined, the sample is mounted in the Universal Test System jaws and sensor values are reset. Both DIC imaging and load cell sample rates are set to 10 Hz to make the two systems compatible during data processing. The DIC image capture is initiated shortly before the tension test to ensure maximum accuracy.

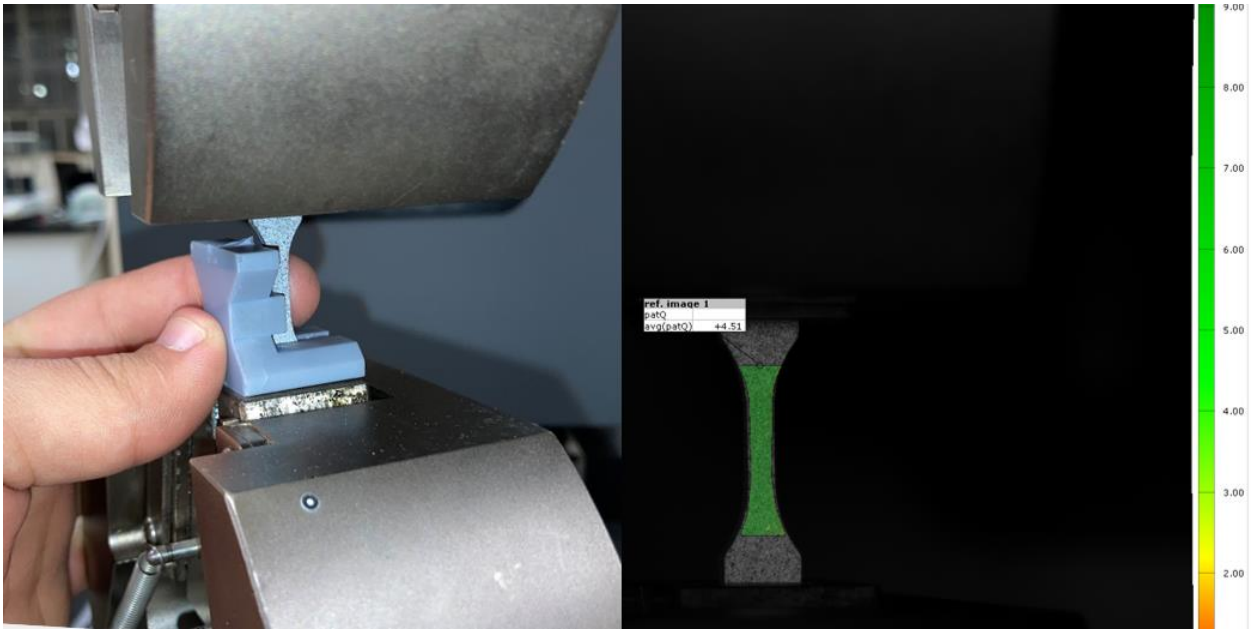

Figure 21: Alignment and Surface Pattern Evaluation

4.2 DIC Data Processing

Upon completion of testing, capturing sequences are terminated and data is output for each specimen. The universal testing system raw data is exported as a .csv file which is prepared for processing by the GOM software suite associated with the DIC. A python script that removes quotation marks (“”) from the raw data file is used to clean data before being imported into the GOM software. The corresponding sample files are merged together and a known time signature is selected as a common point between both data sets, normally the first movement of the crosshead jaws. Once the two files have been combined, a built in script for the specific specimen type is initiated. The script outputs several different “report” pages with different datasets that can be exported. Namely, this includes stress/strain data and material data (Young’s modulus, Poisson-value, and ultimate stress). Output data further evaluated using Microsoft Excel.

4.3 Fracture Geometry Capture

Broken samples also had their fracture geometry captured using the Keyence VL-700 to create a digital twin of each sample. Presented below in *Figure 22*. Surface data was captured of three samples at a time using high magnification, image stitching, and the fine measurement mode. 15 images were captured in $\pm 105°$ from the centerline with manually tuned brightness parameters to minimize glare and maximize resolution of the fracture zone.

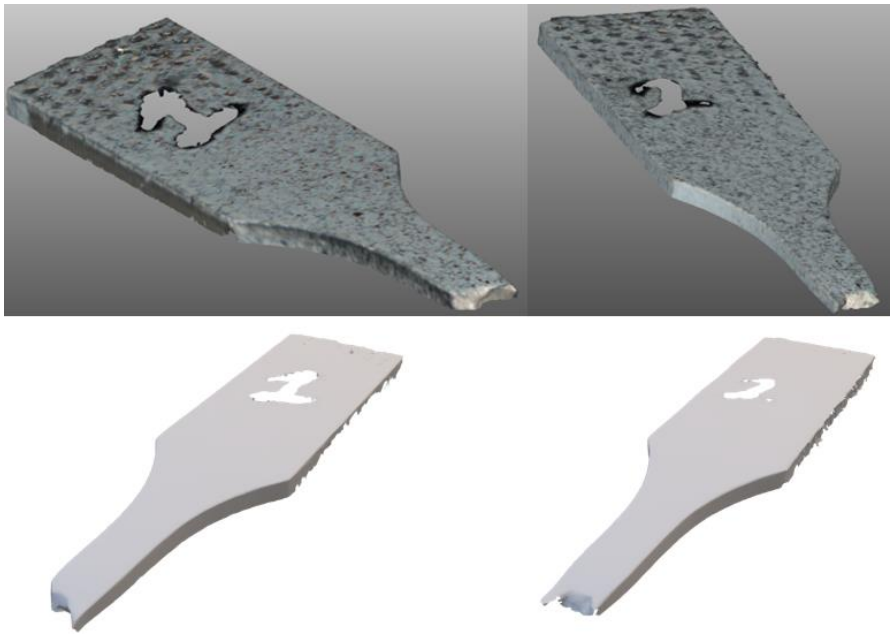

Figure 22: Digital Twin of Broken Samples

While surface geometry is beneficial when using the VL-700 software, STL files provide additional versatility and the ability to evaluate specimen geometry with a variety of tools and software. Regardless, the 3D scanner presents limitations in evaluating more detailed failure modes, necessitating the use of microscopy for additional analysis. To this end, a Keyence VHX-7000 digital microscope was used to image the unpainted surface of each specimen's fracture

such as those shown in *Figure 23* [94]. While 80x magnification is the primary image resolution collected, other magnifications will be addressed in **Chapter 5**.

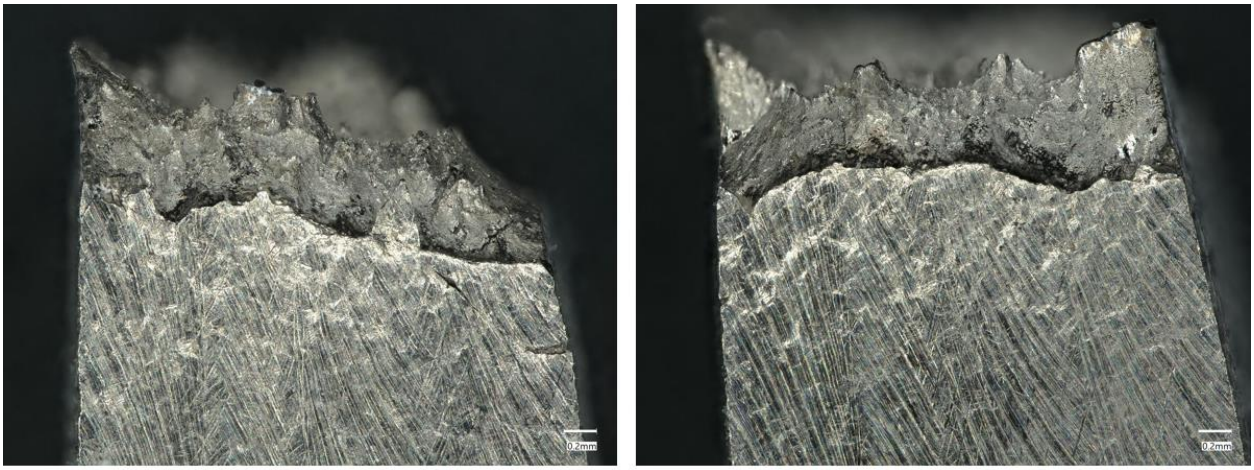

Figure 23: 80x Magnification of Sample Fracture Optical Microscope

A) SR0 S1 **B)** SR0 S2

Chapter 5: Results

5.1 Printing Results

Creating a color map of the residual stresses in the printed samples, and removing S16 as an outlier, results in *Figure 24* below. There appears to be little correlation between the quantity of residual stresses within specimens and build plate location. The only correlation that may be made is that residual stresses are slightly higher for the center of the plate and the lower left corner, S12 - S17, S30*, and S32*. This may be caused by several factors: laser power variations, scanning path inconsistencies, inconsistent EDM removal, and sample variations. Sample variations provide the most likely answer as several of the upper right samples had removed themselves from the build plate along one edge during the printing process and appears to have resulted in asymmetric thermal stress formation across the samples. As mentioned previously, a thin section of the build plate was remove while machining off samples which may be a good indicator for why the bottom half of the plate exhibits higher internal stresses. While laser power variation should not be counted out, additional testing is required as this evaluation has only a single print to evaluate. Additionally, the calculated internal stresses are very high, indicating that one of the simplifications made while evaluating each beam's deflection may be innaccurate. Regardless, the heat map of *Figure 24* strongly aligns with measured deflection values which signify internal stresses.

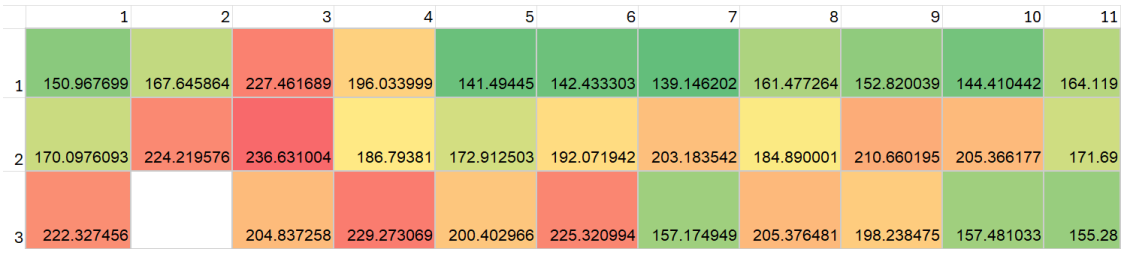

	1	2	3	4	5	6	7	8	9	10	11
1	150.967699	167.645864	227.461689	196.033999	141.49445	142.433303	139.146202	161.477264	152.820039	144.410442	164.119
2	170.0976093	224.219576	236.631004	186.79381	172.912503	192.071942	203.183542	184.890001	210.660195	205.366177	171.69
3	222.327456		204.837258	229.273069	200.402966	225.320994	157.174949	205.376481	198.238475	157.481033	155.28

Figure 24: Heat Map of Residual Stresses and Build Plate Location

5.2 Bulk Material Testing Results

In some alloy systems, hardness is a relatively reliable and cheap method of inspection to determine the results of heat treatment, but this is not recommended for titanium and its alloys because the correlation between strength and hardness is poor [71]. Regardless, an average Rockwell C Scale hardness was evaluated for all 3 samples manufactured along the laser differential line. While data is not directly transferrable between Vickers hardness and Rockwell C hardness, a conversion table and interpolation will be used to permit interpretation of hardness between the GE specifications and in-house testing [95].

Table 12: Limited Hardness Test

Treatment	Specimen Number	Rockwell C (HRC)	HV10
SR0	6	40	382*
SR2	12	35	359*
SR3	24	38	362*
SR0	GE Spec.	37.5*	357
SR1	GE Spec.	35.9*	342

*Indicates a conversion from one type of hardness to the other

These tests were not completed in-house and were instead provided by one of the SAML researchers who has access to additional equipment through Tinker Air Force Base. Unfortunately, there few trends that can be surmised with this data for several reasons. While these values present relatively similar data for SR0, this evidence is coming from a single sample and is the product of converting one hardness measurement into that of another. The

fundamentally unique ways that both hardness tests operate by indicate that future testing should be conducted using the Vickers Hardness test or an inquiry should be made regarding potential information GE may have for Rockwell C hardness tests.

The other mechanical properties of interest, namely modulus of elasticity, 0.2% yield strength, and ultimate tensile strength are presented below in *Tables 13 – 18*7 First, minimum, maximum, mean, standard deviation, and the relevant GE specifications are presented. Second, the mean mechanical properties are presented and compared with the GE specification in *Table 18*. Finally, data regarding the minimum required characteristics for AM titanium per ASTM F3302 and general mechanical properties for treated titanium are presented in *Tables 19 – 21*. Note that values for 0.2% yield strength have extremely high deviation and are notably lower than those presented by the GE data sheet. This is likely caused by several factors surrounding data acquisition and evaluation. Stress and strain data is derived using the GOM metrology software after it has processed load-extension data from the universal testing machine. Determining the synchronization time between the two data sets is completed visually. Setting the synchronization point incorrectly may result in this type of failed analysis. An snapshot of the analysis is included in *Figure 25*.

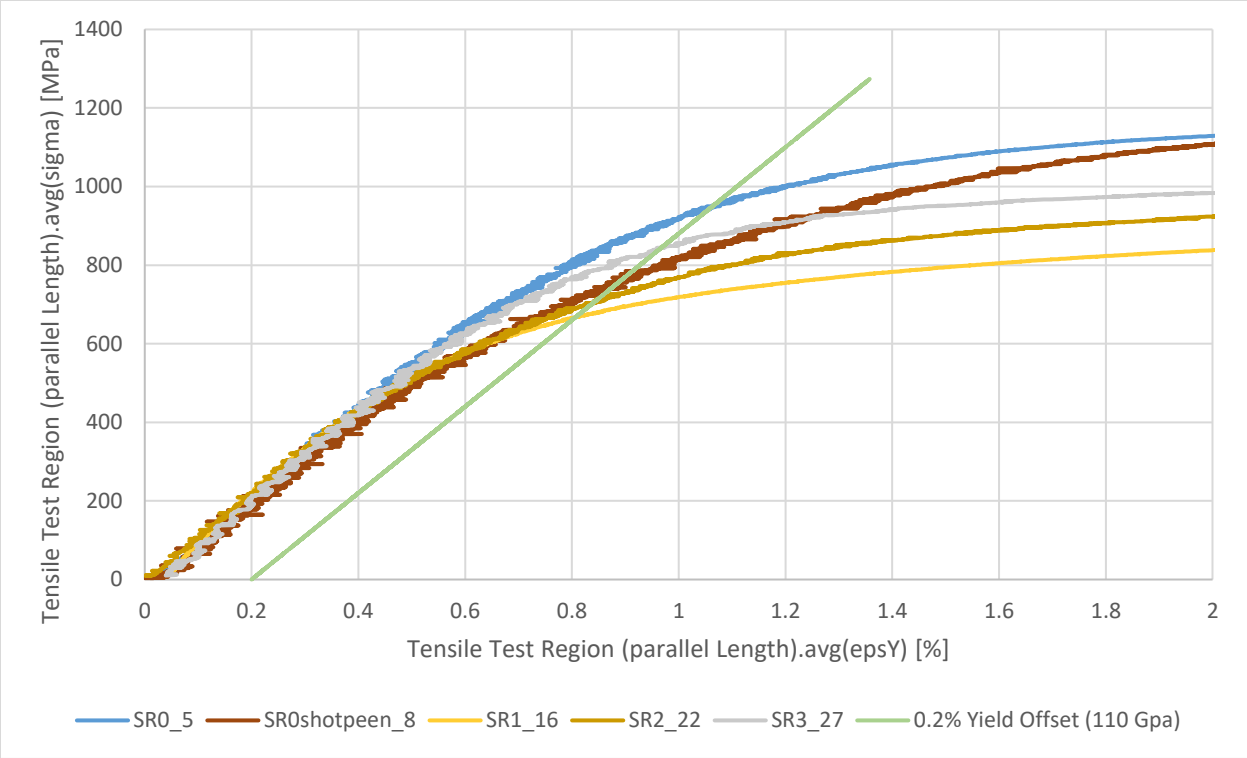

Figure 25: Standard Method of Evaluating 0.2% Yield Stress

Another explanation for substantially lowered yield stress may also be the tested cross-head speed. ASTM F3302 indicates a head speed notably below what was used, 0.003 – 0.007 mm/mm/s compared to the tested 0.5 mm/mm/min (0.0083 mm/mm/s). Using *Figure 25* and *Figure 26*, the geometry of the stress-strain curve may be evaluated. Each specimen presents an elongated elbow, which may be a result of the abnormally high cross-head speed and user error in the time synchronization. Additionally, there may be other causes for anomalous data in the GOM metrology D638 processing script and it may utilize unforeseen parameters that are fundamentally incompatible with the metals.

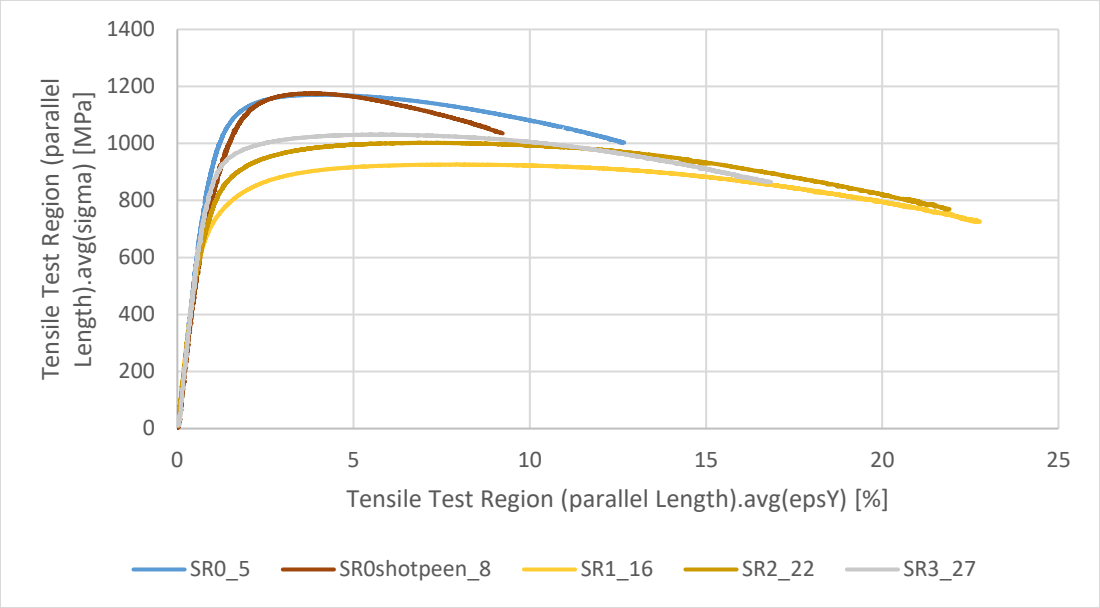

Figure 26: Stress Strain Data Representative for each Treatment Type

Finally, the data is unlikely to perfectly align with GE's material data as the two tests utilize different specimens. Regardless, this study serves to provide an exploratory evaluation of the printed material in unideal circumstances to evaluate shortcomings in specimen processing before processing reaches full capacity. Comparing the properties acquired to the GE specification presents a reasonable picture for the future.

Table 13: SR0 Mechanical Performance (n=7)

Parameter	Minimum	Maximum	Mean	Standard Deviation	GE Value
Young's Modulus (GPa)	107.034	139.027	121.573	10.586	113
0.2% Yield Strength (MPa)	730.608	1105.63	891.758	142.629	1115
Ultimate Tensile Strength (MPa)	1170.75	1260.17	1203.77	33.136	1255
Elongation (%)	11.094	13.845	12.322	0.7887	7
Poisson's Ratio	0.24	0.48	0.337	0.075	-

SR0 reliably presents the highest ultimate tensile strength and yield strength of the 5 sample sets. Namely, the average ultimate tensile strength, Young's modulus, and elongation are relatively close to the GE specifications. Poisson's Ratio is not included in the data sheet, but aligns with expected values for Ti-64. High ultimate tensile strengths and modulus are also attained with that of the shot peened samples as well. The reduction in elongation percentage and Poisson's ratio is to be expected of a cold worked material. The Poisson's ratio value should be interpreted cautiously, as an outlier case resulted in a very low ratio.

Table 14: SR0 Shot Peen Mechanical Performance (n=4)

Parameter	Minimum	Maximum	Mean	Standard Deviation	GE Value
Young's Modulus (GPa)	99.542	130.366	116.867	12.989	113
0.2% Yield Strength (MPa)	576.94	917.183	761.5535	121.498	1115
Ultimate Tensile Strength (MPa)	1133.92	1187.1	1163.528	20.061	1255
Elongation (%)	8.915	9.296	9.140	0.145	7
Poisson's Ratio	0.04	0.44	0.195	0.161	-

Another note on the performance of the shot peened samples is that the treatment procedure reduced the thickness of the material, in some cases visibly so. This left much to be desired of the test and presents an avenue that requires additional research before large scale applications are implemented.

Table 15: SR1 Mechanical Performance (n=6)

Parameter	Minimum	Maximum	Mean	Standard Deviation	GE Value
Young's Modulus (GPa)	124.840	163.480	143.468	16.849	121
0.2% Yield Strength (MPa)	486.955	680.649	599.713	58.154	940
Ultimate Tensile Strength (MPa)	919.59	999.18	941.244	29.25	1015
Elongation (%)	14.274	22.775	20.042	3.020	16
Poisson's Ratio	0.17	0.32	0.243	0.048	-

SR1 provided some of the most promising results regarding microstructure changes and their visibility under the microscope, but slightly under-performed compared to expectations. It is possible that the heat treatment did not cool rapidly enough to precipitate the desired quantity of alpha phase in the grain structure. The GE data sheet does not specify a cooling rate which is an important characteristic of the treatment process. *Figure 27* outlines the achieved material properties from a variety of cooling times but is generally in reference to solution treatments.

Table 16: SR2 Mechanical Performance (n=6)

Parameter	Minimum	Maximum	Mean	Standard Deviation	GE Value
Young's Modulus (GPa)	98.551	216.570	140.71	38.822	118
0.2% Yield Strength (MPa)	209.701	859.531	598.05	211.606	995
Ultimate Tensile Strength (MPa)	979.46	1016.98	998.13	13.196	1050
Elongation (%)	18.863	21.983	20.70	1.342	13.5
Poisson's Ratio	0.28	0.4	0.32	0.042426	-

Table 17: SR3 Mechanical Performance (n=6)

Parameter	Minimum	Maximum	Mean	Standard Deviation	GE Value
Young's Modulus (GPa)	114.032	155.504	124.482	14.189	119
0.2% Yield Strength (MPa)	660.353	840	773.828	61.883	1080
Ultimate Tensile Strength (MPa)	1015.23	1078.95	1041.503	19.33101	1135
Elongation (%)	11.311	16.845	14.958	1.830	12
Poisson's Ratio	0.22	0.34	0.303	0.039	-

A similar trend is presented in both SR2 and SR3. Once again, it is important to note that these processes do not have an outlined cooling rate and are left as "furnace cooled" in the data sheet.

Table 18: Mean Mechanical Performance

Parameter	Young's Modulus (GPa)	0.2% Yield Strength (MPa)	Ultimate Tensile Strength (MPa)	Elongation (%)	Poisson's Ratio
SR0	121.573	891.758	1203.77	12.322	0.337
GE SR0	113	1115	1255	7	-
SR1	143.468	599.713	941.244	20.042	0.243
GE SR1	121	940	1015	16	-
SR2	140.713	598.053	998.13	20.697	0.32
GE SR2	118	995	1050	13.5	-
SR3	124.482	773.828	1041.503	14.958	0.303
GE SR3	119	1080	1135	12	-
SR0 Shot Peen	116.867	761.5535	1163.528	9.140	0.195

Evaluating the entirety of the tensile data, several trends may be outlined. First, samples consistently present a higher elongation percentage at fracture than that the outlined GE specification and is indicative of high-density titanium. A similar trend can be made for the calculated Young's modulus. Ultimate tensile strength approaches that of the data set, with the greatest shortfall appearing SR3. Additionally, the mean Poisson's ratio is consistent with expected values for Ti-64 for SR0, SR2, and SR3, with lower than anticipated ratios in SR1 and the shot peening batch. Excluding the 0.2% yield strength values, the requirements for AM Ti-64, presented in *Table 19*, were met, or exceeded for all processing parameters.

Table 19: Minimum Mechanical Properties ASTM F3302-18 [96]

Material	Tensile Strength (MPa)	Yield Strength at 0.2% Offset (MPA)	Elongation in 50 mm or 4D (%)
CP Ti	450	380	18
Ti-6Al-4V	895	825	10
Ti-6Al-4V ELI	860	795	10

While this indicates that the GE Additive Concept M2 Series 5 Titanium Ti-64 Grade 23 SLM printer and its treated parts can uphold the standards of ASTM F3302, the material performance leaves more to be desired of the material in subsequent testing. Performance metrics may be better compared to those found in *Table 4* and *Table 5* for solution treated Ti-64. While additional processing does occur during the solution treatment process (quenching and aging), the treatment temperatures and performance are comparable to those of SR1 and SR2 for solution treatment and SR3 for annealing or high temperature stress relief.

The significance of the heat treatment process cannot be understated as the residual stresses held within printed parts are relatively large when large surface areas are used in conjunction with the build plate. This begs the question of thermal treatment and sample size with the transition from ASTM D638 Type V samples to ASTM E8 round samples. *Table 20* outlines some expected trends for increasing the sample size, but is primarily in reference to solution treatment processes. This trend indicates the relationship between grain formation, alpha-beta precipitates, and thermal inertia. Sufficiently large parts should take these considerations into account when evaluating the type of heat treatment completed and the expected performance of the component.

Table 20: Tensile Strength of Heat Treated Titanium Alloys for Various Sized Square Bar Sections [71]

Alloy	13 mm (MPa)	25 mm (MPa)	50 mm (MPa)	75 mm (MPa)	100 mm (MPa)	150 mm (MPa)
Ti-6Al-4V	1105	1070	1000	930	---	---
Ti-6Al-2Sn-4Zr-6Mo	1170	1170	1170	1140	1105	---
Ti-10V-2Fe-3Al	1240	1240	1240	1240	1170	1170
Ti-13V-11Cr-3Al	1310	1310	1310	1310	1310	1310

For in-lab purposes, heat treatment cooling rates will need to be determined so as to standardize material expectations. *Figure 27* indicates this trend well with the material characteristics of Ti-64 as a function of cooling delay. Standardizing this cooling rate is likely to bridge the gap between expected material properties of AM parts with the data sheet and point to the mechanism that makes SR0 the strongest treatment option.

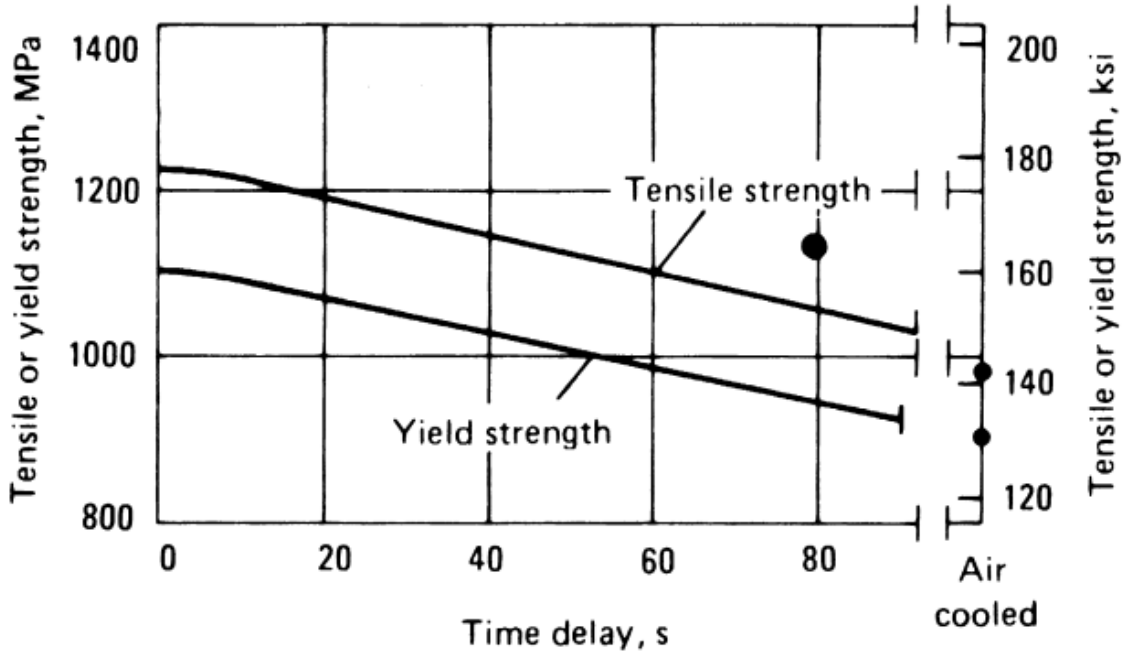

Figure 27: Mechanical Properties of Cooled Ti-64 [71]

5.3 Oxidation Study

Alongside gaining better control over and standardizing furnace cooling rates, a more refined method of oxidation protection will need to be developed. *Figure 28* shows the appearance of SR1, SR2, and SR3 after they completed their respective heat treatments. Of the three studies, SR1 received the least severe oxidation as illustrated in *Figure 29*. While the top

surface of each batch was severely oxidized, the bottom surface of SR1 received a gradient of heat treatment. Each color indicates a different level of oxidation.

Figure 28: *Stock Oxidation SR1, SR2, SR3*

A) SR1 **B)** SR2 **C)** SR3

The oxidation characteristics for the most easily recognizable specimen, S17, were capture using the VL-700 3D scanner. This process is the result of the highest flow rate for the shortest period of time. Since the bottom of the samples were left partially oxidized or completely unoxidized in the center, it is possible that increasing argon flow rate will sufficiently protect the samples.

Figure 29: Bottom Face of SR1 After Heat Treatment

Reviewing the Nabertherm catalogue, alternative methods of protecting components form oxidation, such as charcoal baths may be necessary as the material cost of each heat treatment is ~1 bottle of argon at 20 SCFH for the heat treatment alone. Increasing the flow rate will require multiple argon bottles and the necessary system to combine them. Alternative solutions may involve the use of a high temperature stopper cap on the gas outlet or improved fiber gaskets. Regardless, ensuring samples are protected from atmospheric conditions is essential if parts are to be used as printed with heat treatment. Oxidized parts not only form the brown scale along the surface of titanium components, but also present reduced mechanical properties. Oxidized parts must have their outer surface machined based on maximum exposed temperature and time of exposure as the samples presented in this experiment were. Machining should meet or exceed requirements outlined by ASM International [71].

5.4 Microscopy Results

Polished samples were evaluated at a consistent magnification using full coaxial lighting and partial coaxial lighting at a consistent magnification. As illustrated in *Figure* 30, visible damage directly decreases as the particle size decreases. *Figures 30 A – C* illustrate surface roughness dominated by deep gouges generated by the abrasive material. At 1μm deformation from abrasives is still visible, but the presence of particles presents a larger obstruction to the sample surface. Figure 30 E presents a much more even surface than previous images, but the face is still dominated by pocketing and hard-to-remove particles. Previous polishing processes concluded the procedure with the 0.05 μm particle and successful images were taken using SEM. However, the surface roughness generated in does not permit accurate imaging of Ti-64

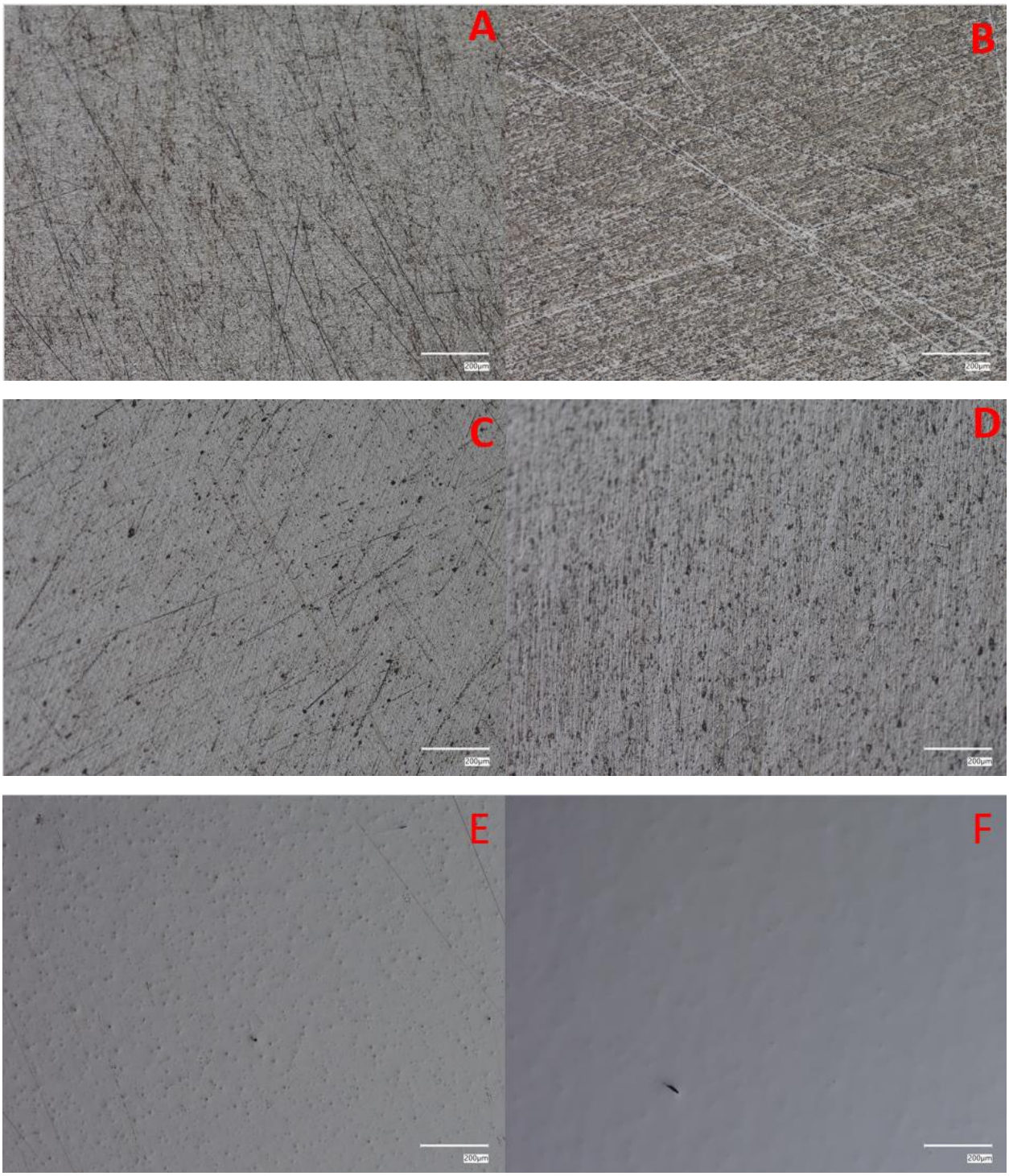

Figure 30: Grinding Surface Appearance 200x Optical

A) *9* μ*m polish* ***B)*** *6* μ*m polish* ***C)*** *3* μ*m polish* ***D)*** *1* μ*m polish* ***E)*** *0.05* μ*m polish* ***F)*** *0.02* μ*m polish*

Incorporating the final particle size, 0.02 μm, creates a sufficiently flat surface to observe the lamellar structure of the alpha- beta- phases. While these structures are slightly visible using full coaxial lighting, they become more prevalent with the use of partial coaxial lighting. Additionally, the VHX-7000 offers a digital enhancement called “optical shadow effect” which dramatically increases the visibility of the fine structure of Ti-64.

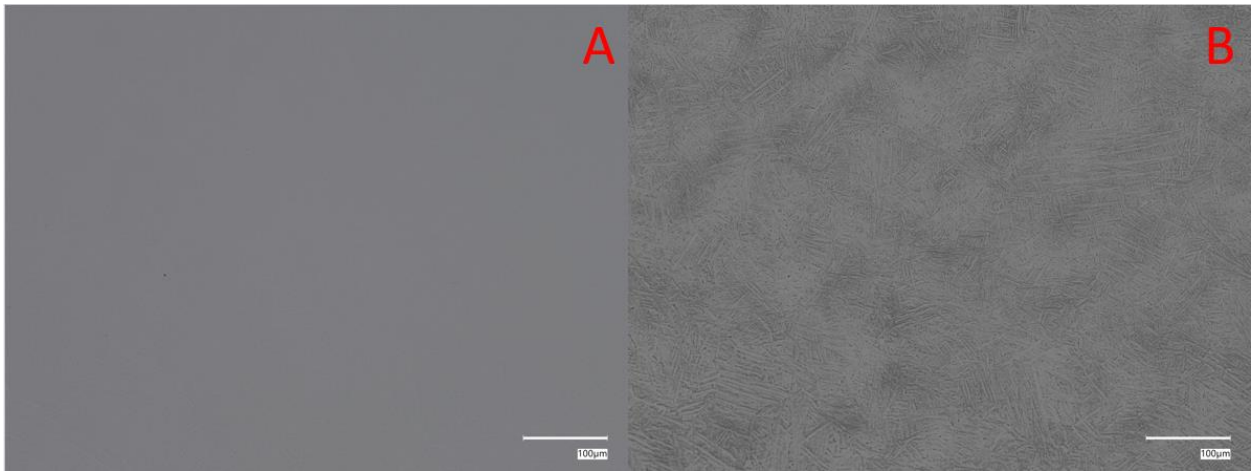

Figure 31: *400x Partial Coaxial Lighting SR2 S21*

A) *Partial coaxial lighting alone* ***B)*** *Partial coaxial lighting with optical shadow effect*

Subsequent imaging primarily makes use of the optical shadow effect at various magnifications to determine the feasibility of using optical microscopy as a means to analyze grain characteristics of Ti-64. *Figures 32 – 35* present visible grain characteristics at varying magnitudes. Of particular importance is *Figure 33*. SR1 is the only heat treatment that has micrographs presented by GE in the titanium data sheet which presents the opportunity to compare in-house SR1 samples with that of GE’s data. The heat treatment SR1 has a noticeable effect on the size of the columnar alpha precipitates, indicating successful modification of the microstructure, which mechanical testing also agrees with.

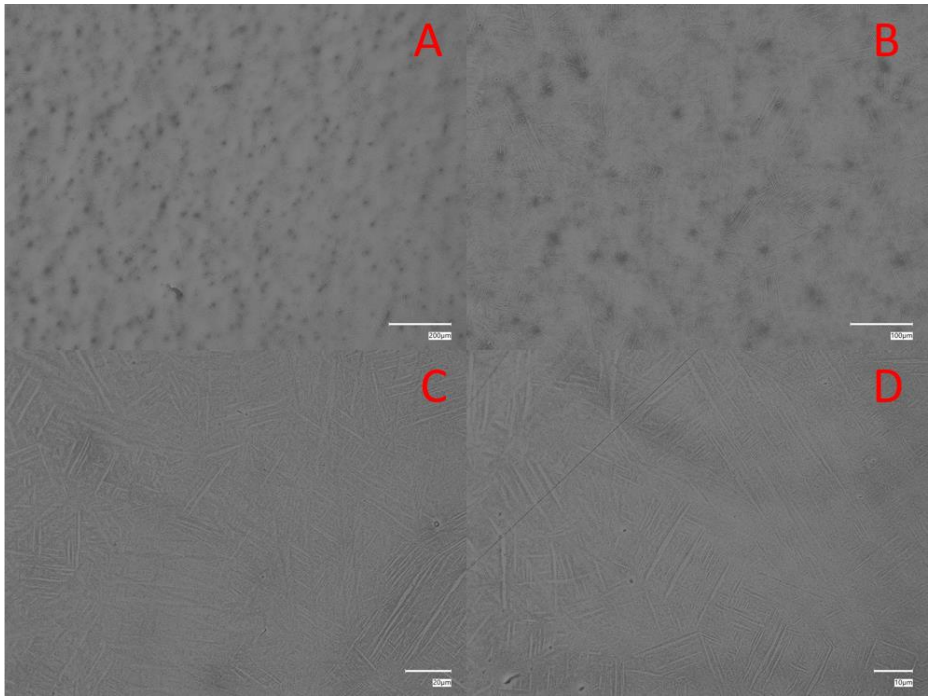

Figure 32: SR0 S1 Partial Coaxial with Optical Shadow

A) *200x* ***B)*** *400x* ***C)*** *1500x* ***D)*** *2500x*

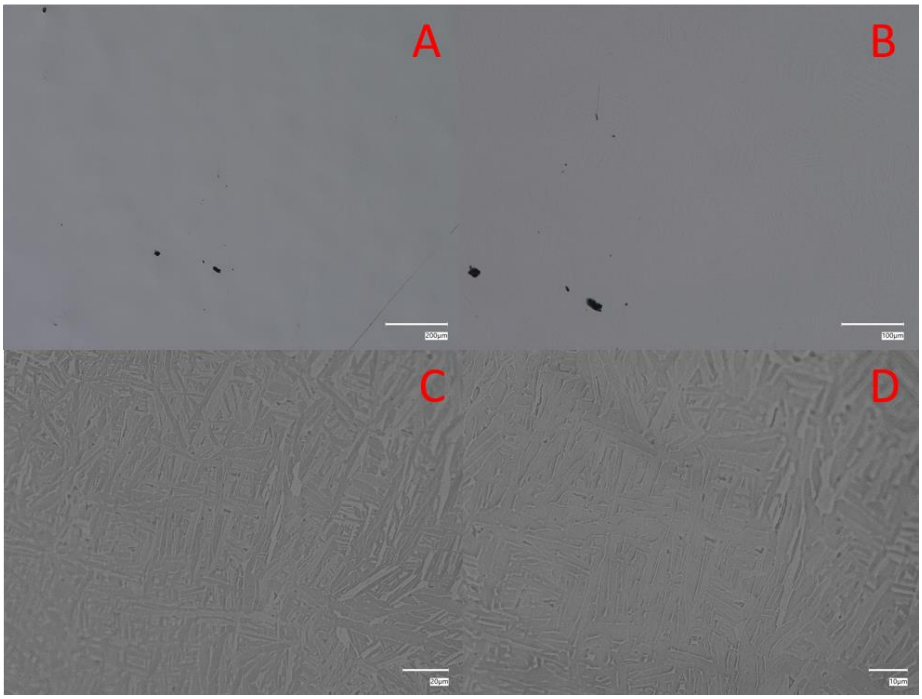

Figure 33: *SR1 S17 Partial Coaxial with Optical Shadow*

A) *200x* ***B)*** *400x* ***C)*** *1500x* ***D)*** *2500x*

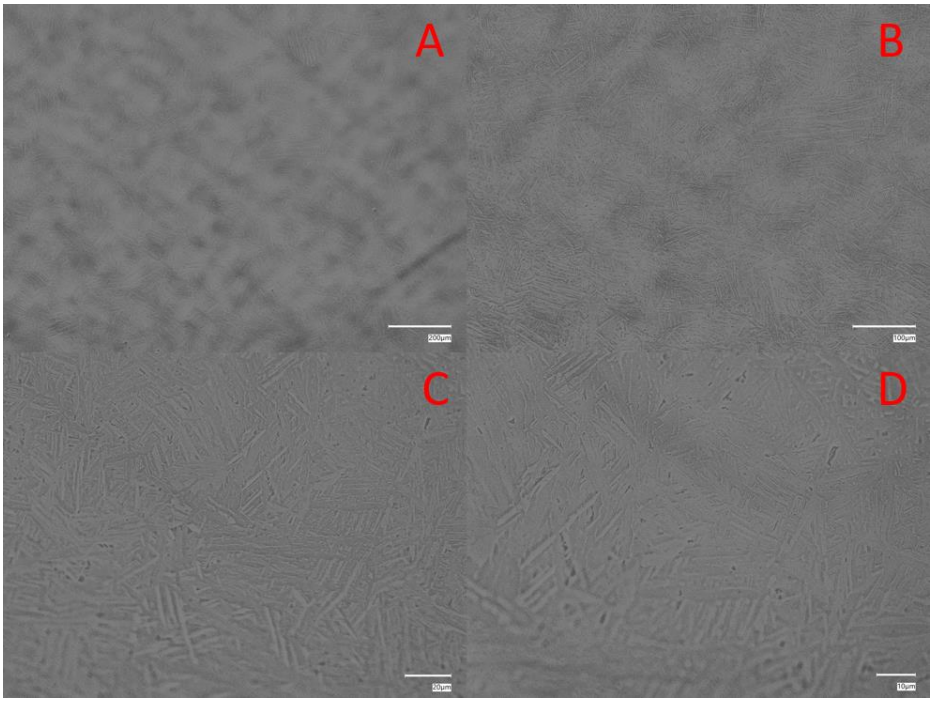

Figure 34: SR2 S21 Partial Coaxial with Optical Shadow

A) *200x* ***B)*** *400x* ***C)*** *1500x* ***D)*** *2500x*

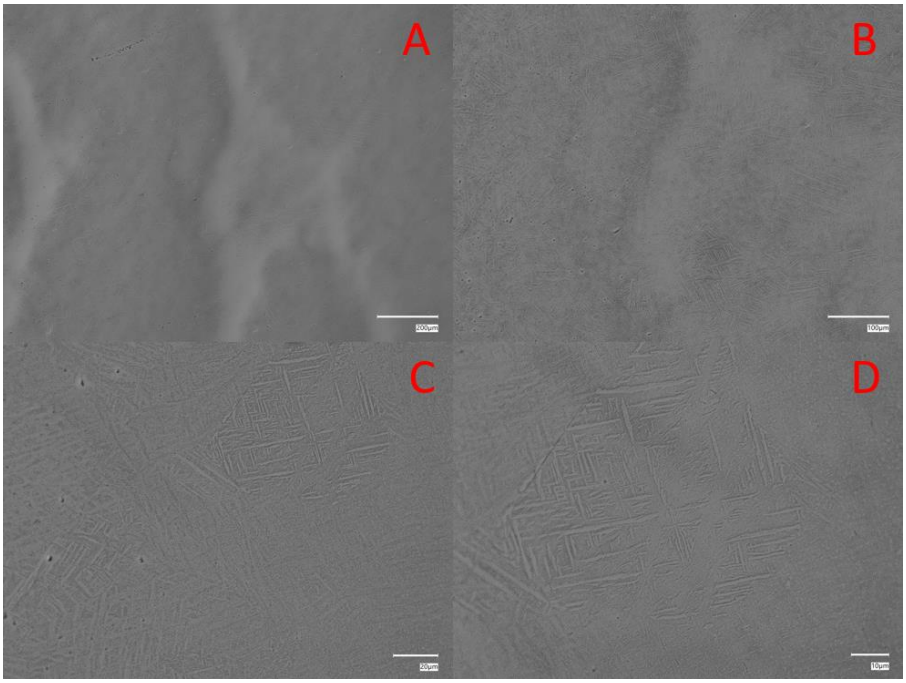

Figure 35: *SR3 S26 Partial Coaxial with Optical Shadow*

A) *200x* ***B)*** *400x* ***C)*** *1500x* ***D)*** *2500x*

CUI

To confirm the accuracy of optical imagery, SEM micrographs were also taken of the same samples: SR0 S1, SR1 S17, SR2 S21, and SR3 S26. Findings are shown below in *Figure 36* curtesy of Ben Sherwood.

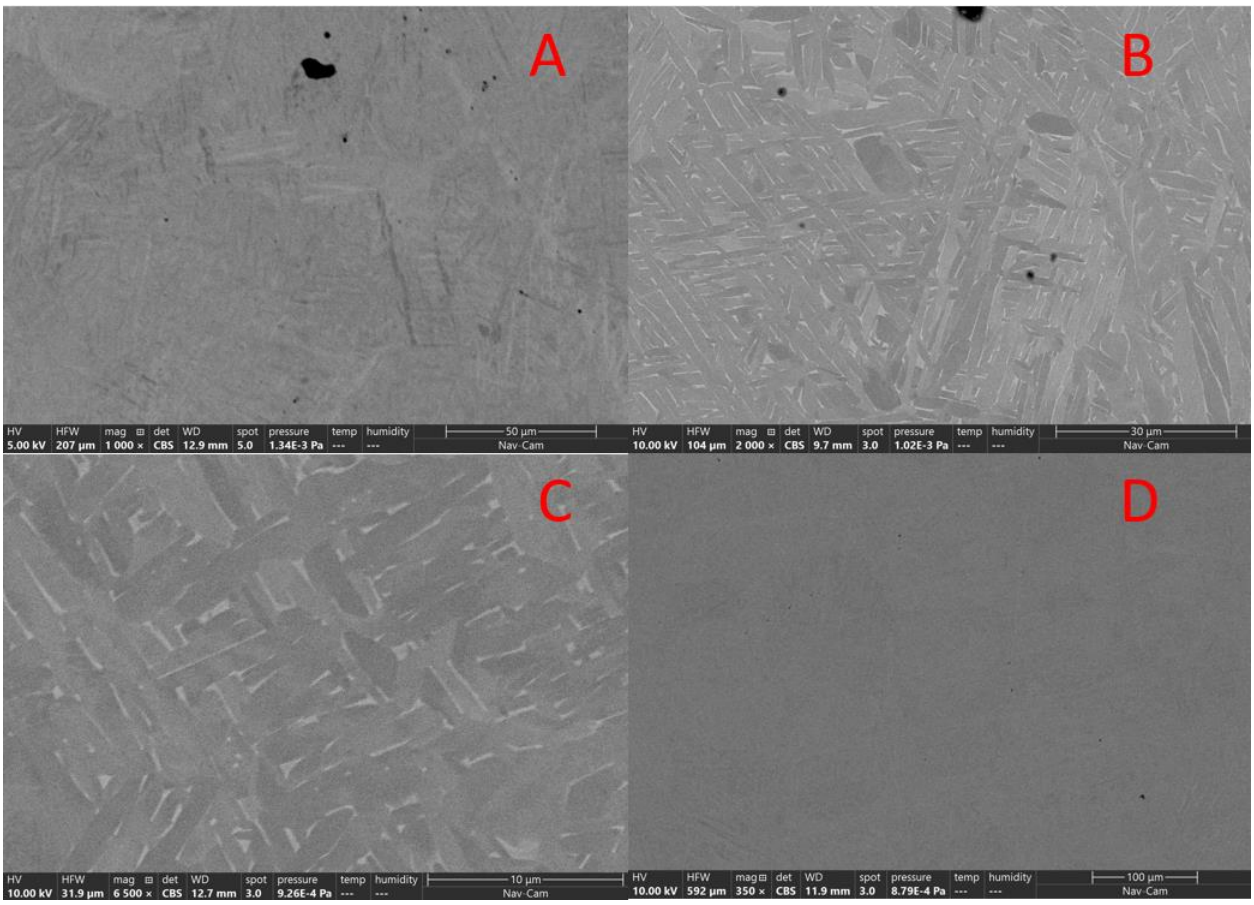

Figure 36: *SEM Images of SR0, SR1, SR2, and SR3 Samples*

A) *SR0 S1* ***B)*** *SR1 S17* ***C)*** *SR2 S21* ***D)*** *SR3 S26*

Comparisons of *Figure 36* with *Figures 32-35* results in an understanding that SEM is necessary for more detailed analysis. While optical images may present a viable method for determining whether SR1 has sufficiently treated a part, the fine structure present in SR0, SR2, and SR3 make it much more challenging to distinguish between treated and untreated structures.

Additionally, optical images are limited in the amount of information they may provide regarding chemical composition and grain orientation unlike SEM.

5.4.1 Fracture Modes

While optical microscopy is limited to surface features, this is sufficient to determine that samples are failing as expected. Using STL files and surface geometry shown in *Figure 22*, high magnification images shown in *Figure 23*, and high-resolution depth composition images shown in *Figure 37*, the failure mode may be analyzed.

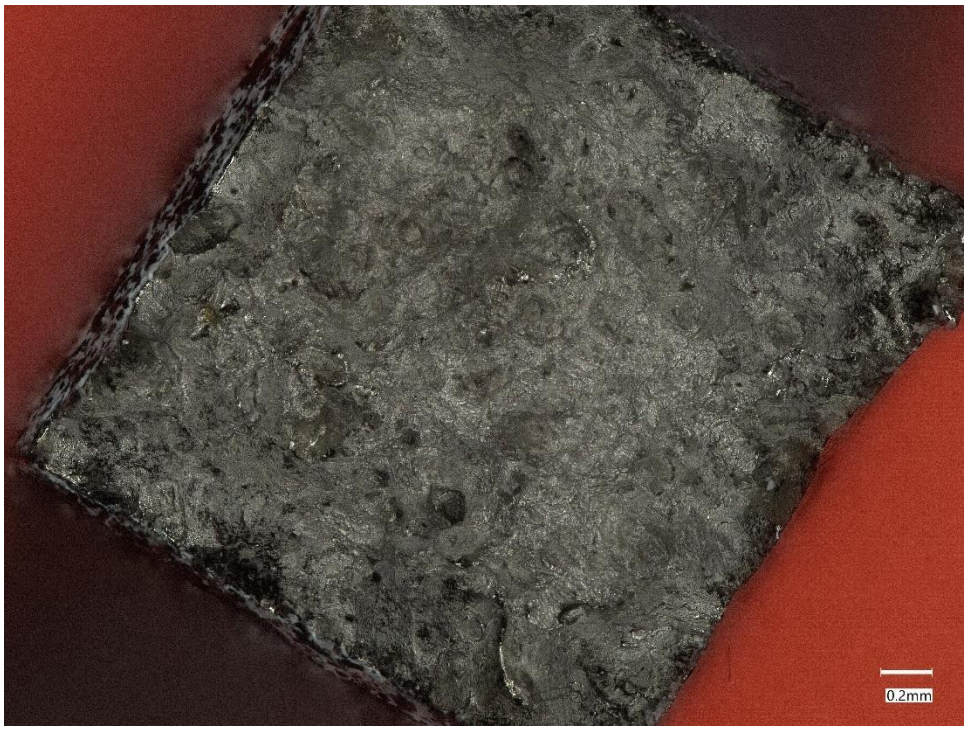

Figure 37: *SR0 S1 Fracture Surface Top View 80x Depth Composition*

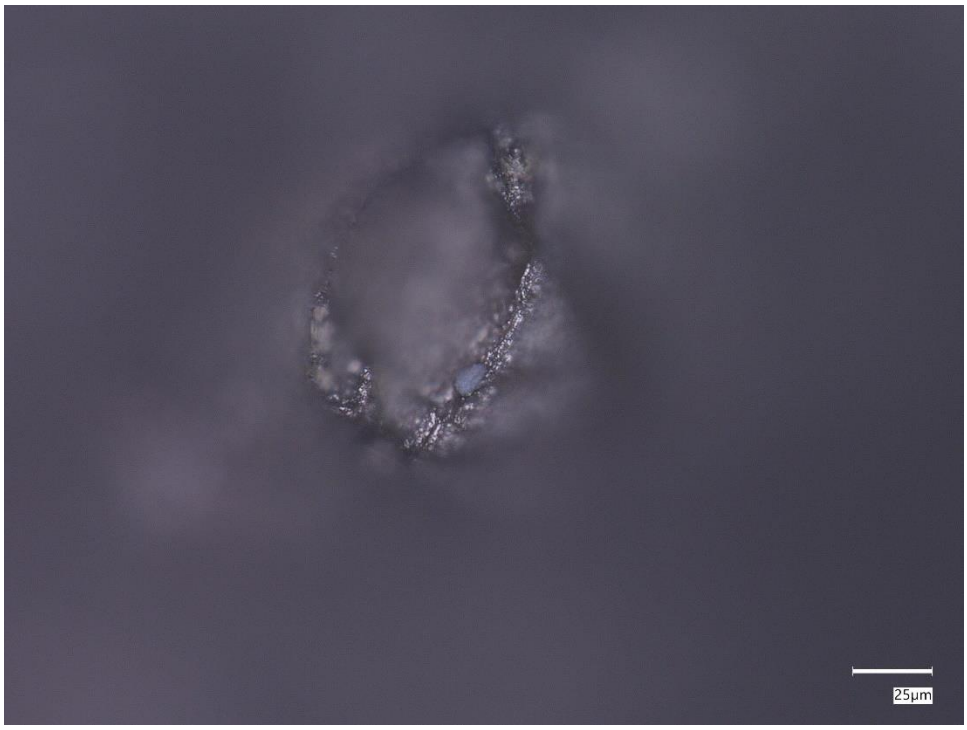

Figure 38: *SR0 S1 Fracture Surface Top View 1000x Crack Nucleation Site*

Top view images provide a high-fidelity view of the pocketed surface formed in the center of each sample. Titanium is a low- to moderately- ductile material at room temperature and becomes increasingly ductile at elevated temperatures. Since all tests were performed at room temperature, aspects of ductile failure are present, particularly in the center of test specimen cross-sections.

Using 3-dimensional image capture of the fracture areas, aspects of cup and cone failure as well as shear failure are more easily visualized than with surface data and micrographs alone. Combining *Figure 39* with the other images of SR0 S1 and material failure theory of low- to moderately- ductile materials, a general description of the specimen failure mode can be made.

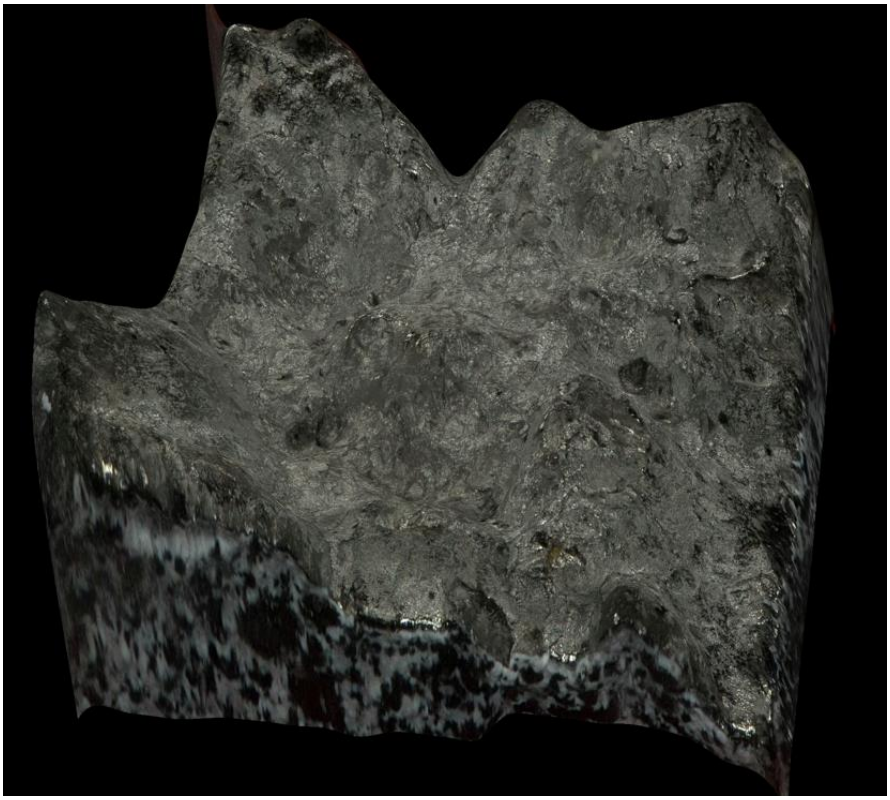

Figure 39: SR0 S1 80x Magnification 3D Image

The fracture for SR0 S1 samples exhibits a necked cross-section, a cup and or cone formation within the center of the specimen, and shear failure along the outer edges. Necking creates additional stress in the center of the material where void nucleation begins. As stress increases, voids coalesce, forming the pock-marked surface and pocketing in the center of the specimen. As the crack propagates, the cross-sectional area is reduced and shearing dominates the remaining failure, resulting in ~45° failure along the perimeter of the sample. This results in failure surfaces that appear to look like domes or bowls surrounded by more steeply angles walls. The geometry of each fracture correlates with the sample ductility. Comparing *Figure 39* to *Figure 40* it is noticeable that more ductile treatments result in more ductile failures.

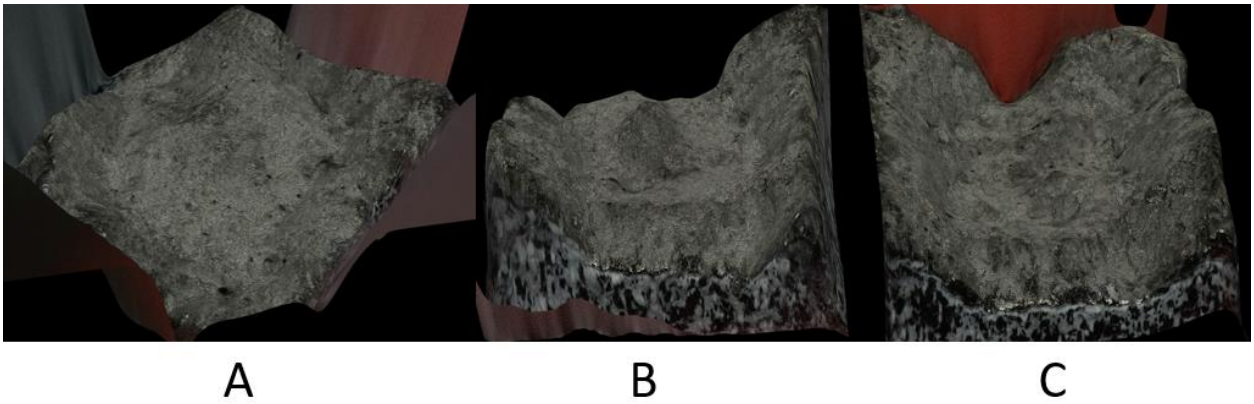

Figure 40: 80x Magnification 3D Images

A) SR1 S17 **B)** SR2 S21 **C)** SR3 S26

While all specimens exhibited some level of shearing at the fracture surface, these were lease prevalent in SR1, the most ductile of the heat treatments. SR0, SR2, and SR3 exhibit similar behavior with SR0 shot peen being the least ductile and resulting in failures that look like *Figure 41*. These failures are quite brittle and have elongation at fracture characteristics that coincide with this fracture mode.

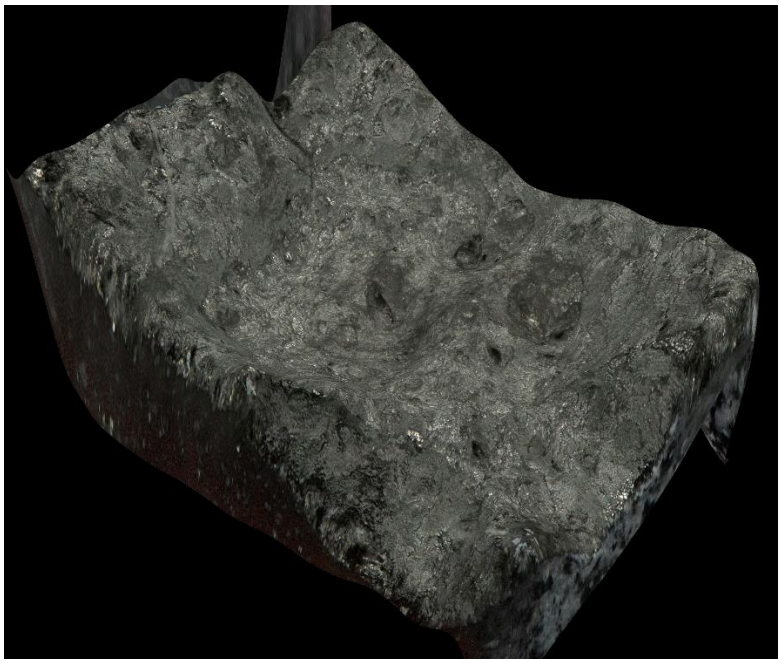

Figure 41: SR0 Shot Peen 80x Magnification 3D Image

Chapter 6: Conclusions and Future Work

6.1 Material Properties

While several of the key material properties did not meet expectations, this is likely caused by an overestimation of Young's modulus in the ASTM D638 macro and inadequate synchronization of the tensile machine data and the DIC data. Subsequent samples will be using the correct ASTM E8 macro for metals which is compatible with the material being studied. In the case of this study, the limited material available requires the use smaller samples machined to an alternative specification. Manual re-evaluation of the DIC results and tensile data should be completed to better evaluate this specific data set. Regardless, Poisson's ratio, ultimate tensile strength, and elongation percentage at fracture all present results that align with the manufacturer's specifications and or comparably treated Ti-64 samples. Differences in material properties are likely caused by errors in the evaluation or treatment process and or caused by print failure.

Future assessments should complete a single specimen trial to evaluate the performance of the ASTM E8 macro before processing samples en masse to ensure that DIC data does not need to be manually evaluated. Subsequent testing should utilize a strain rate of 0.003 - 0.007 mm/mm/min per ASTM F3302-18 instead of those used by Baufeld and Biest and Foehring as this rate best aligns with ASTM standards and, likely, Air Force requirements [92], [93], [96]. Similarly, subsequent hardness studies should be modified to be of the Vickers Hardness test instead of the Rockwell C hardness test to ensure consistency with manufacturer specification. Future studies will complete testing and evaluation with many more samples and a modified process compared to that presented in this study. However, the basic principles and shortcomings

should be evaluated to create improved processes going forward. Capturing surface data of samples after printing, machining, treatment, and fracture is good practice that thoroughly documents specimen characteristics from cradle to grave. The same can be said for intentionally creating batch samples that have the same treatment history as test specimens for microscopy.

6.2 Oxidization

While the oxidization study presented here is limited, the resulting evidence is clear; an alternative strategy to prevent oxidation is necessary. If this becomes a time constraint and it is necessary to move on without a robust solution, increasing specimen size and removing stock from the samples becomes essential. Resources like ASM International's handbook on nonferrous alloys should be reviewed by new lab members to ensure that the team has a strong background in the relevant material science in the case of accidental oxidations or for improved experiment design. Still, several strategies for preventing oxidation have yet to be explored and should be evaluated before resorting to increased material expenditure.

6.3 Microscopy

With the addition of new polishing equipment at the SAML, a new procedure will need to be designed. However, the above outlined procedure should both be maintained as a record for successful Ti-64 preparation and as a basis for new procedures. Optimizing particle step-down sizes has proved valuable and utilizing a finer particle during the finishing process has consistently yielded results with the current equipment. Ti-64 microstructure became visible with optical microscopy, but limitedly so. Without a strong understanding of the intended microstructure for the GE heat treatments and what those may look like, the application of the optical microscope will be limited to fracture analysis and observing lamella geometry using the

optical shadow feature. For more in-depth research, SEM should be utilized more thoroughly alongside the presented polishing process or an improved polishing process. Depending on the detail in which microscopic data should be evaluated, considerations should be made for polishing test specimens before testing to evaluate changes and damage in grain structure at the fracture point. Further investigation in chemical or electrical etching and optical microscopy should be considered, but detailed EBSD measurements using SEM and other imaging may prove more valuable depending on the overarching goals of the microscopy.

References

[1] I. Gibson, D. Rosen, and B. Stucker, *Additive manufacturing technologies: 3D printing, rapid prototyping and direct digital manufacturing*, Second Edition. New York Heidelberg Dodrecht London: Springer, 2015.

[2] B. Berman, "3-D printing: The new industrial revolution," *Bus. Horiz.*, vol. 55, no. 2, pp. 155–162, Mar. 2012, doi: 10.1016/j.bushor.2011.11.003.

[3] M. Gebler, A. J. M. Schoot Uiterkamp, and C. Visser, "A global sustainability perspective on 3D printing technologies," *Energy Policy*, vol. 74, pp. 158–167, Nov. 2014, doi: 10.1016/j.enpol.2014.08.033.

[4] C. Deckard, "Method and apparatus for producing parts by selective sintering," US4863538A, Sep. 05, 1989 [Online]. Available: https://patents.google.com/patent/US4863538A/en

[5] N. Guo and M. C. Leu, "Additive manufacturing: technology, applications and research needs," *Front. Mech. Eng.*, vol. 8, no. 3, pp. 215–243, Sep. 2013, doi: 10.1007/s11465-013-0248-8.

[6] "Polymers For 3D Printing | EOS," EOS GmbH. Accessed: Apr. 04, 2024. [Online]. Available: https://www.eos.info/en-us/polymer-solutions/polymer-materials

[7] "High Performance PEKK Polymer Materials for Industrial 3D Printing | EOS," EOS GmbH. Accessed: Apr. 04, 2024. [Online]. Available: https://www.eos.info/en-us/polymer-solutions/polymer-materials/high-performance

[8] "Rapid manufacturing and prototyping options extended." Accessed: Apr. 04, 2024. [Online]. Available: https://www.plasticstoday.com/plastics-processing/rapid-manufacturing-and-prototyping-options-extended

[9] M. J. Jackson, J. Kopac, M. Balazic, D. Bombac, M. Brojan, and F. Kosel, "Titanium and Titanium Alloy Applications in Medicine," in *Surgical Tools and Medical Devices*, W. Ahmed and M. J. Jackson, Eds., Cham: Springer International Publishing, 2016, pp. 475–517. doi: 10.1007/978-3-319-33489-9_15.

[10] Y. Bai *et al.*, "Characterization, corrosion behavior, cellular response and in vivo bone tissue compatibility of titanium–niobium alloy with low Young's modulus," *Mater. Sci. Eng. C*, vol. 59, pp. 565–576, Feb. 2016, doi: 10.1016/j.msec.2015.10.062.

[11] "ASM Material Data Sheet." Accessed: Apr. 04, 2024. [Online]. Available: https://asm.matweb.com/search/SpecificMaterial.asp?bassnum=mtp641

[12] B. Vandenbroucke and J. Kruth, "Selective laser melting of biocompatible metals for rapid manufacturing of medical parts," *Rapid Prototyp. J.*, vol. 13, no. 4, pp. 196–203, Aug. 2007, doi: 10.1108/13552540710776142.

[13] C. Y. Yap *et al.*, "Review of selective laser melting: Materials and applications," *Appl. Phys. Rev.*, vol. 2, no. 4, p. 041101, Dec. 2015, doi: 10.1063/1.4935926.

[14] J. Wilkes, Y. Hagedorn, W. Meiners, and K. Wissenbach, "Additive manufacturing of ZrO_2-Al_2O_3 ceramic components by selective laser melting," *Rapid Prototyp. J.*, vol. 19, no. 1, pp. 51–57, Jan. 2013, doi: 10.1108/13552541311292736.

[15] H. Gong, K. Rafi, H. Gu, T. Starr, and B. Stucker, "Analysis of defect generation in Ti–6Al–4V parts made using powder bed fusion additive manufacturing processes," *Addit. Manuf.*, vol. 1–4, pp. 87–98, Oct. 2014, doi: 10.1016/j.addma.2014.08.002.

[16] I. Yadroitsev, Ph. Bertrand, and I. Smurov, “Parametric analysis of the selective laser melting process,” *Appl. Surf. Sci.*, vol. 253, no. 19, pp. 8064–8069, Jul. 2007, doi: 10.1016/j.apsusc.2007.02.088.

[17] I. Yadroitsev, I. Yadroitsava, P. Bertrand, and I. Smurov, “Factor analysis of selective laser melting process parameters and geometrical characteristics of synthesized single tracks,” *Rapid Prototyp. J.*, vol. 18, no. 3, pp. 201–208, Apr. 2012, doi: 10.1108/13552541211218117.

[18] L. Zhang and H. Attar, “Selective Laser Melting of Titanium Alloys and Titanium Matrix Composites for Biomedical Applications: A Review,” *Adv. Eng. Mater.*, vol. 18, no. 4, pp. 463–475, Apr. 2016, doi: 10.1002/adem.201500419.

[19] B. Gao, H. Zhao, L. Peng, and Z. Sun, “A Review of Research Progress in Selective Laser Melting (SLM),” *Micromachines*, vol. 14, no. 1, p. 57, Dec. 2022, doi: 10.3390/mi14010057.

[20] M. Niinomi, *Metals for biomedical devices*, 2nd ed. in Woodhead publishing series in biomaterials. Duxford: Woodhead publishing, 2019.

[21] H. Attar, M. Calin, L. C. Zhang, S. Scudino, and J. Eckert, “Manufacture by selective laser melting and mechanical behavior of commercially pure titanium,” *Mater. Sci. Eng. A*, vol. 593, pp. 170–177, Jan. 2014, doi: 10.1016/j.msea.2013.11.038.

[22] M. Drexler, M. Lexow, and D. Drummer, “Selective Laser Melting of Polymer Powder – Part Mechanics as Function of Exposure Speed,” *Phys. Procedia*, vol. 78, pp. 328–336, 2015, doi: 10.1016/j.phpro.2015.11.047.

[23] H. Irrinki *et al.*, “Effects of Powder Attributes and Laser Powder Bed Fusion (L-PBF) Process Conditions on the Densification and Mechanical Properties of 17-4 PH Stainless Steel,” *JOM*, vol. 68, no. 3, pp. 860–868, Mar. 2016, doi: 10.1007/s11837-015-1770-4.

[24] A. Chalancon and D. Bourell, “Measured Energy Desnsities for Polyamide 12 and Comparision of Values Calculated for Laser Sintering,” in *Applications*, University of Texas in Austin, Austin Texas, United States: University of Texas in Austin, Aug. 2016, p. 2217. Accessed: Apr. 05, 2024. [Online]. Available: https://utw10945.utweb.utexas.edu/sites/default/files/2016/177-Chalancon.pdf

[25] F. Lupone, E. Padovano, F. Casamento, and C. Badini, “Process Phenomena and Material Properties in Selective Laser Sintering of Polymers: A Review,” *Materials*, vol. 15, no. 1, p. 183, Dec. 2021, doi: 10.3390/ma15010183.

[26] J.-P. Kruth, B. Van Der Schueren, J. E. Bonse, and B. Morren, “Basic Powder Metallurgical Aspects in Selective Metal Powder Sintering,” *CIRP Ann.*, vol. 45, no. 1, pp. 183–186, 1996, doi: 10.1016/S0007-8506(07)63043-1.

[27] J. Kruth, P. Mercelis, J. Van Vaerenbergh, L. Froyen, and M. Rombouts, “Binding mechanisms in selective laser sintering and selective laser melting,” *Rapid Prototyp. J.*, vol. 11, no. 1, pp. 26–36, Feb. 2005, doi: 10.1108/13552540510573365.

[28] N. K. Tolochko, Yu. V. Khlopkov, S. E. Mozzharov, N. V. Sobolenko, and I. A. Yadroitsev, “Measurement of the absorption coefficient of freely poured one-component metallic powders and its change during laser sintering,” *Powder Metall. Met. Ceram.*, vol. 36, no. 7–8, pp. 433–437, Jul. 1997, doi: 10.1007/BF02676008.

[29] T. Laumer, T. Stichel, K. Nagulin, and M. Schmidt, “Optical analysis of polymer powder materials for Selective Laser Sintering,” *Polym. Test.*, vol. 56, pp. 207–213, Dec. 2016, doi: 10.1016/j.polymertesting.2016.10.010.

[30] S. E. Brika, M. Letenneur, C. A. Dion, and V. Brailovski, “Influence of particle morphology and size distribution on the powder flowability and laser powder bed fusion manufacturability of Ti-6Al-4V alloy,” *Addit. Manuf.*, vol. 31, p. 100929, Jan. 2020, doi: 10.1016/j.addma.2019.100929.

[31] H. Attar *et al.*, “Effect of Powder Particle Shape on the Properties of In Situ Ti–TiB Composite Materials Produced by Selective Laser Melting,” *J. Mater. Sci. Technol.*, vol. 31, no. 10, pp. 1001–1005, Oct. 2015, doi: 10.1016/j.jmst.2015.08.007.

[32] J. Zhang *et al.*, “Influence of Particle Size on Laser Absorption and Scanning Track Formation Mechanisms of Pure Tungsten Powder During Selective Laser Melting,” *Engineering*, vol. 5, no. 4, pp. 736–745, Aug. 2019, doi: 10.1016/j.eng.2019.07.003.

[33] E. Hecht, *Optics*, 5 ed/fifth edition, Global edition. Boston Columbus Indianapolis New York San Francisco Amsterdam Cape Town Dubai London Madrid Milan Munich: Pearson, 2017.

[34] Z. Xiaoyan, “Scanning Algorithm for 3D Laser Carving System,” *J. Eng. Graph.*, 2007, [Online]. Available: https://api.semanticscholar.org/CorpusID:112740882

[35] J. W. Xie, P. Fox, W. O’Neill, and C. J. Sutcliffe, “Effect of direct laser re-melting processing parameters and scanning strategies on the densification of tool steels,” *J. Mater. Process. Technol.*, vol. 170, no. 3, pp. 516–523, Dec. 2005, doi: 10.1016/j.jmatprotec.2005.05.055.

[36] F. Geiger, K. Kunze, and T. Etter, “Tailoring the texture of IN738LC processed by selective laser melting (SLM) by specific scanning strategies,” *Mater. Sci. Eng. A*, vol. 661, pp. 240–246, Apr. 2016, doi: 10.1016/j.msea.2016.03.036.

[37] H. Shu-huai, “Programming and Realization of a Compound Scanpath in Selective Laser Sintering,” 2004. [Online]. Available: https://api.semanticscholar.org/CorpusID:113063576

[38] Y.-M. Huang and C.-P. Jiang, “Curl Distortion Analysis During Photopolymerisation of Stereolithography Using Dynamic Finite Element Method,” *Int. J. Adv. Manuf. Technol.*, vol. 21, no. 8, pp. 586–595, Jun. 2003, doi: 10.1007/s00170-002-1317-z.

[39] Y. Jin, Y. He, and J. Du, “A novel path planning methodology for extrusion-based additive manufacturing of thin-walled parts,” *Int. J. Comput. Integr. Manuf.*, vol. 30, no. 12, pp. 1301–1315, Dec. 2017, doi: 10.1080/0951192X.2017.1307526.

[40] Z. Snow, A. R. Nassar, and E. W. Reutzel, “Invited Review Article: Review of the formation and impact of flaws in powder bed fusion additive manufacturing,” *Addit. Manuf.*, vol. 36, p. 101457, Dec. 2020, doi: 10.1016/j.addma.2020.101457.

[41] E. M. Sefene, “State-of-the-art of selective laser melting process: A comprehensive review,” *J. Manuf. Syst.*, vol. 63, pp. 250–274, Apr. 2022, doi: 10.1016/j.jmsy.2022.04.002.

[42] L. Thijs, F. Verhaeghe, T. Craeghs, J. V. Humbeeck, and J.-P. Kruth, “A study of the microstructural evolution during selective laser melting of Ti–6Al–4V,” *Acta Mater.*, vol. 58, no. 9, pp. 3303–3312, May 2010, doi: 10.1016/j.actamat.2010.02.004.

[43] H. Jia, H. Sun, H. Wang, Y. Wu, and H. Wang, “Scanning strategy in selective laser melting (SLM): a review,” *Int. J. Adv. Manuf. Technol.*, vol. 113, no. 9–10, pp. 2413–2435, Apr. 2021, doi: 10.1007/s00170-021-06810-3.

[44] Y. Lu *et al.*, “Study on the microstructure, mechanical property and residual stress of SLM Inconel-718 alloy manufactured by differing island scanning strategy,” *Opt. Laser Technol.*, vol. 75, pp. 197–206, Dec. 2015, doi: 10.1016/j.optlastec.2015.07.009.

[45] J. Li *et al.*, “Microstructure and performance optimisation of stainless steel formed by laser additive manufacturing,” *Mater. Sci. Technol.*, vol. 32, no. 12, pp. 1223–1230, Aug. 2016, doi: 10.1080/02670836.2015.1114774.

[46] A. T. Clare, P. R. Chalker, S. Davies, C. J. Sutcliffe, and S. Tsopanos, “Selective laser melting of high aspect ratio 3D nickel–titanium structures two way trained for MEMS applications,” *Int. J. Mech. Mater. Des.*, vol. 4, no. 2, pp. 181–187, Jun. 2008, doi: 10.1007/s10999-007-9032-4.

[47] C. K. Chua and K. F. Leong, *3D Printing and Additive Manufacturing: Principles and Applications (with Companion Media Pack)Fourth Edition of* Rapid Prototyping, 4th ed. WORLD SCIENTIFIC, 2014. doi: 10.1142/9008.

[48] R. Li, J. Liu, Y. Shi, L. Wang, and W. Jiang, “Balling behavior of stainless steel and nickel powder during selective laser melting process,” *Int. J. Adv. Manuf. Technol.*, vol. 59, no. 9–12, pp. 1025–1035, Apr. 2012, doi: 10.1007/s00170-011-3566-1.

[49] P. Krakhmalev and I. Yadroitsev, “Microstructure and properties of intermetallic composite coatings fabricated by selective laser melting of Ti–SiC powder mixtures,” *Intermetallics*, vol. 46, pp. 147–155, Mar. 2014, doi: 10.1016/j.intermet.2013.11.012.

[50] M. Sigl, S. Lutzmann, and M. F. Zaeh, “Transient Physical Effects in Electron Beam Sintering,” Sep. 2006, doi: 10.26153/TSW/7154.

[51] M. Kahnert, S. Lutzmann, and M. F. Zaeh, “Layer formations in electron beam sintering,” *18th Solid Free. Fabr. Symp. SFF 2007*, pp. 88–99, Jan. 2007.

[52] H. P. Tang, G. Y. Yang, W. P. Jia, W. W. He, S. L. Lu, and M. Qian, “Additive manufacturing of a high niobium-containing titanium aluminide alloy by selective electron beam melting,” *Mater. Sci. Eng. A*, vol. 636, pp. 103–107, Jun. 2015, doi: 10.1016/j.msea.2015.03.079.

[53] C. Guo, F. Lin, W. Ge, and J. Zhang, *Development of Novel EBSM System for High-Tech Material Additive Manufacturing Research*. 2014.

[54] C. Körner, “Additive manufacturing of metallic components by selective electron beam melting — a review,” *Int. Mater. Rev.*, vol. 61, no. 5, pp. 361–377, Jul. 2016, doi: 10.1080/09506608.2016.1176289.

[55] L. E. Murr *et al.*, “Fabrication of Metal and Alloy Components by Additive Manufacturing: Examples of 3D Materials Science,” *J. Mater. Res. Technol.*, vol. 1, no. 1, pp. 42–54, Apr. 2012, doi: 10.1016/S2238-7854(12)70009-1.

[56] C. Guo, “Study on the Fabrication Process of 316L Stainless Steel via Electron Beam Selective Melting,” *J. Mech. Eng.*, vol. 50, no. 21, p. 152, 2014, doi: 10.3901/JME.2014.21.152.

[57] L. M. Sochalski-Kolbus *et al.*, “Comparison of Residual Stresses in Inconel 718 Simple Parts Made by Electron Beam Melting and Direct Laser Metal Sintering,” *Metall. Mater. Trans. A*, vol. 46, no. 3, pp. 1419–1432, Mar. 2015, doi: 10.1007/s11661-014-2722-2.

[58] M. Ramsperger, L. Mújica Roncery, I. Lopez-Galilea, R. F. Singer, W. Theisen, and C. Körner, “Solution Heat Treatment of the Single Crystal Nickel-Base Superalloy CMSX-4 Fabricated by Selective Electron Beam Melting,” *Adv. Eng. Mater.*, vol. 17, no. 10, pp. 1486–1493, Oct. 2015, doi: 10.1002/adem.201500037.

[59] T. E. Everhart and P. H. Hoff, “Determination of Kilovolt Electron Energy Dissipation vs Penetration Distance in Solid Materials,” *J. Appl. Phys.*, vol. 42, no. 13, pp. 5837–5846, Dec. 1971, doi: 10.1063/1.1660019.

[60] H. E. Helmer, C. Körner, and R. F. Singer, "Additive manufacturing of nickel-based superalloy Inconel 718 by selective electron beam melting: Processing window and microstructure," *J. Mater. Res.*, vol. 29, no. 17, pp. 1987–1996, Sep. 2014, doi: 10.1557/jmr.2014.192.

[61] X. Gong, T. Anderson, and K. Chou, "Review on powder-based electron beam additive manufacturing technology," *Manuf. Rev.*, vol. 1, p. 2, 2014, doi: 10.1051/mfreview/2014001.

[62] S. Tammas-Williams, H. Zhao, F. Léonard, F. Derguti, I. Todd, and P. B. Prangnell, "XCT analysis of the influence of melt strategies on defect population in Ti–6Al–4V components manufactured by Selective Electron Beam Melting," *Mater. Charact.*, vol. 102, pp. 47–61, Apr. 2015, doi: 10.1016/j.matchar.2015.02.008.

[63] N. Hrabe and T. Quinn, "Effects of processing on microstructure and mechanical properties of a titanium alloy (Ti–6Al–4V) fabricated using electron beam melting (EBM), Part 2: Energy input, orientation, and location," *Mater. Sci. Eng. A*, vol. 573, pp. 271–277, Jun. 2013, doi: 10.1016/j.msea.2013.02.065.

[64] "M2SERIES5_TI64_CMDS_20220516_RevC.pdf." Accessed: Apr. 05, 2024. [Online]. Available: https://www.ge.com/additive/sites/default/files/2022-05/M2SERIES5_TI64_CMDS_20220516_RevC.pdf

[65] "SVM series," DN Solutions. Accessed: Apr. 05, 2024. [Online]. Available: https://www.dn-solutions.com/en/product/machining-center/vertical/svm-4100.do

[66] "Renishaw OMP60 Probe Kit (legacy)," RenishawProbe. Accessed: Apr. 09, 2024. [Online]. Available: https://renishawprobe.com/p/machine-tool/A-4038-0001

[67] American Society for Testing and Materials International, "Standard Test Methods for Tension Testing of Metallic Materials." American Society of Testing and Materials ASTM International, 100 Barr Harbor Drive, PO Box C700, West Conshohocken, PA 19428-2959, United States.

[68] American Society for Testing and Materials International, "Standard Test Method for Tensile Properties of Plastics." ASTM International, 100 Barr Harbor Drive, PO Box C700, West Conshohocken, PA 19428-2959, United States, 2022.

[69] "Out of Production 5900 Series Universal Testing Systems." Accessed: Apr. 06, 2024. [Online]. Available: https://www.instron.com/en/products/testing-systems/universal-testing-systems/low-force-universal-testing-systems/5900-series

[70] "ARAMIS Adjustable: The modular measuring system for 2D and 3D analysis." Accessed: Apr. 06, 2024. [Online]. Available: https://www.gom.com/en/products/3d-testing/aramis-adjustable

[71] M. J. Donachie, *Titanium: a technical guide*, 2nd ed. Materials Park, OH: ASM International, 2000.

[72] "thermalprocesstechnology2_english.pdf." Accessed: Apr. 07, 2024. [Online]. Available: https://nabertherm.com/sites/default/files/2023-08/thermalprocesstechnology2_english.pdf

[73] Society of Automotive Engineers, "AEROSPACE MATERIAL SPECIFICATION AMS2750™." SAE International, Jun. 2022.

[74] "SparkFun RedBoard Artemis Nano - DEV-15443 - SparkFun Electronics." Accessed: Apr. 07, 2024. [Online]. Available: https://www.sparkfun.com/products/15443

[75] "SparkFun High Precision Temperature Sensor - TMP117 (Qwiic) - SEN-15805 - SparkFun Electronics." Accessed: Apr. 07, 2024. [Online]. Available: https://www.sparkfun.com/products/15805

[76] “SparkFun Qwiic Thermocouple Amplifier - MCP9600 (PCC Connector) - SEN-16294 - SparkFun Electronics.” Accessed: Apr. 07, 2024. [Online]. Available: https://www.sparkfun.com/products/16294
[77] Y. Zhang, J. Li, S. Che, and Y. Tian, “Electrochemical Polishing of Additively Manufactured Ti–6Al–4V Alloy,” *Met. Mater. Int.*, vol. 26, no. 6, pp. 783–792, Jun. 2020, doi: 10.1007/s12540-019-00556-0.
[78] “Metallography of titanium and titanium alloys insight | Struers.com.” Accessed: Apr. 07, 2024. [Online]. Available: https://www.struers.com/en/Knowledge/Materials/Titanium#grindingpolishing
[79] “Subsurface Damage.” Accessed: Apr. 07, 2024. [Online]. Available: https://www.edmundoptics.com/knowledge-center/application-notes/lasers/subsurface-damage/
[80] “Grinding and Polishing Guide - Buehler - Metallography Equipment & Supplies for Sample Preparation.” Accessed: Apr. 07, 2024. [Online]. Available: https://www.buehler.com/blog/grinding-and-polishing-guide/
[81] “PG - EpoxyMount v1.7.pdf.” Accessed: Apr. 07, 2024. [Online]. Available: https://www.alliedhightech.com/Media/Default/images/PG%20-%20EpoxyMount%20v1.7.pdf
[82] “LaboSystem fast and reliable modular grinding and polishing system | Struers.com.” Accessed: Apr. 07, 2024. [Online]. Available: https://www.struers.com/en/Products/Grinding-and-Polishing/Grinding-and-polishing-equipment/LaboSystem
[83] “Diamond Suspensions Glycol Based Polycrystalline - Allied High Tech Products.” Accessed: Apr. 07, 2024. [Online]. Available: https://consumables.alliedhightech.com/Diamond-Suspensions-Glycol-Based-Polycrystalline-p/diagly-poly.htm
[84] “Water Based Diamond Suspensions - Monocrystalline.” Accessed: Apr. 07, 2024. [Online]. Available: https://consumables.alliedhightech.com/Water-Based-Diamond-Suspensions-Monocrystalline-p/diawtr-mono.htm
[85] “FinalPrep Alumina Polishing Solution.” Accessed: Apr. 07, 2024. [Online]. Available: https://consumables.alliedhightech.com/FinalPrep-Alumina-Polishing-Solution-p/finprep.htm
[86] “New EDMMax 656W Fast Wire EDM for Sale at EDM Network.” Accessed: Apr. 07, 2024. [Online]. Available: https://www.edmnetwork.com/listings/4738615-edmmax-656w-fast-wire-edm
[87] “2129-AOS-Calipers.pdf.” Accessed: Apr. 07, 2024. [Online]. Available: https://www.mitutoyo.com/webfoo/wp-content/uploads/2129-AOS-Calipers.pdf
[88] “3D Scanner CMM - VL-700 series | KEYENCE America.” Accessed: Apr. 07, 2024. [Online]. Available: https://www.keyence.com/products/measure-sys/3d-scanner/vl-700/
[89] S. Sj, “PORTABLE SURFACE ROUGHNESS TESTER”.
[90] J. Champaigne, “Shot Peening Process Variables.”.
[91] “Colloidal Silica Suspension.” Accessed: Apr. 08, 2024. [Online]. Available: https://consumables.alliedhightech.com/Colloidal-Silica-Suspension-p/collsil05.htm

[92] B. Baufeld and O. Van Der Biest, “Mechanical properties of Ti-6Al-4V specimens produced by shaped metal deposition,” *Sci. Technol. Adv. Mater.*, vol. 10, no. 1, p. 015008, Jan. 2009, doi: 10.1088/1468-6996/10/1/015008.

[93] D. Foehring, H. B. Chew, and J. Lambros, “Characterizing the tensile behavior of additively manufactured Ti-6Al-4V using multiscale digital image correlation,” *Mater. Sci. Eng. A*, vol. 724, pp. 536–546, May 2018, doi: 10.1016/j.msea.2018.03.091.

[94] “Digital Microscope - VHX-7000 series | KEYENCE America.” Accessed: Apr. 08, 2024. [Online]. Available: https://www.keyence.com/products/microscope/digital-microscope/vhx-7000/

[95] “Conversion Chart Of Vickers Hardness (HV) to Rockwell C (HRC).” Accessed: Apr. 08, 2024. [Online]. Available: http://www.taylorspecialsteels.co.uk/pages/main/conchart.htm

[96] American Society for Testing and Materials, “Standard for Additive Manufacturing – Finished Part Properties – Standard Specification for Titanium Alloys via Powder Bed Fusion1.” ASTM Internatinoal, 100 Barr Harbor Drive, PO Box C700, West Conshohocken, PA 19428-2959, United States, 2018.